Robust and Low-Complexity Timing Synchronization for DCO-OFDM LiFi Systems

Robust and Low-Complexity Timing Synchronization for DCO-OFDM LiFi Systems

Yufei Jiang, *Member, IEEE*, Yunlu Wang, *Student Member, IEEE*, Pan Cao, *Member, IEEE*, Majid Safari, *Member, IEEE*, John Thompson, *Fellow, IEEE*, and Harald Haas, *Senior Member, IEEE*

***Abstract*— Light fidelity (LiFi), using light devices like light emitting diodes (LEDs) and visible light spectrum between 400 and 800 THz, provides a new layer of wireless connectivity within existing heterogeneous radio frequency wireless networks. Link data rates of 10 Gbps from a single transmitter have been demonstrated under ideal laboratory conditions. Synchronization is one of these issues usually assumed to be ideal. However, in a practical deployment, this is no longer a valid assumption. Therefore, we propose for the first time a low-complexity maximum likelihood-based timing synchronization process that includes frame detection and sampling clock synchronization for direct current-biased optical orthogonal frequency division multiplexing LiFi systems. The proposed timing synchronization structure can reduce the high-complexity 1-D search to two low-complexity 1-D searches for frame detection and sampling clock synchronization. By employing a single training block, frame detection can be realized, and then sampling clock offset (SCO) and channels can be estimated jointly. We propose a number of three frame detection approaches, robust against the combined effects of both SCO and the low-pass characteristic of LEDs. Furthermore, we derive the Cramér–Rao lower bounds (CRBs) of SCO and channel estimations, respectively. In order to minimize the CRBs and improve synchronization performance, a single training block is designed based on the optimization of training sequences, the selection of training length, and the selection of dc bias. Therefore, the designed training block allows us to analyze the tradeoffs between estimation accuracy, spectral efficiency, energy efficiency, and complexity. The proposed timing synchronization mechanism demonstrates low complexity and robustness benefits and provides performance significantly better than existing methods.**

***Index Terms*— Light fidelity (LiFi), sampling clock offset (SCO), frame detection, timing synchronization, DCO-OFDM.**

I. Introduction

A. Background and Motivation

THE exponentially increasing demand of mobile data traffic is saturating the spectral resources in the conventional radio frequency (RF) networks [1]–[3]. A potential solution to this spectral bottle-neck is to use high carrier frequency for wireless communications, with a large bandwidth utilized [4]. Light fidelity (LiFi) [5], which uses an extremely wide visible light spectrum for high speed communications, has recently been into the focus, and is considered as a promising technology for future networks. It has been shown in [6] that LiFi can achieve data rates up to 14 Gbps using off-the-shelf light emitting diodes (LEDs). The intensity of the light at the output of LEDs can be rapidly changed/modulated to transmit data information and to provide illumination simultaneously.

The main limitation on the data rate of LiFi systems is caused by the low bandwidth of phosphor-coated LEDs, and can cause inter-symbol interference (ISI) when using standard pulsed modulation techniques such as on-off keying (OOK). Orthogonal frequency division multiplexing (OFDM) in conjunction with bit-and-power loading [7] is an effective solution, and has also been widely used for RF systems to combat multipath fading, due to high spectrum efficiency and low-complexity channel equalization. Therefore, OFDM can be applied to solve the problem of ISI caused by LEDs for LiFi systems. OFDM allows transformation of signals between the frequency domain and the time domain by the use of inverse discrete Fourier transform (IDFT) and discrete Fourier transform (DFT). M-ary quadrature amplitude modulation (M-QAM) symbols can be mapped into a number of subcarriers for transmissions. However, complex-valued and bipolar signals are generated in the time domain, which is not applicable for intensity modulation direct detection (IM/DD) LiFi sysems, as intensity modulation optical signals are real and non-negative. This problem can partly be solved by imposing the constraint of Hermitian symmetry, resulting in real-valued signals in the time domain. However, the time-domain signals would be still negative and bipolar, which requires other techniques to make them unipolar before transmissions.

So far, there have been a number of techniques to generate unipolar OFDM signals. Direct current biased optical OFDM (DCO-OFDM) [7]–[9] is one of common techniques. A positive DC bias is introduced, and added to the time-domain signals. By clipping the negative parts of the DC biased signals, the resulting signals are non-negative and unipolar. In fact, the LED requires a level of DC bias for illumination, which can also be used to generate unipolar OFDM signals for transmissions. Asymmetrically clipped optical OFDM (ACO-OFDM) [7], [8] is another modulation technique to generate unipolar signals by clipping entire negative signals. By the appropriate selection of subcarriers, the impairment from clipping noise can be avoided. However, only a quarter of bandwidth in ACO-OFDM signals can be used to transmit data.

Manuscript February 22, 2017; July 15, 2017; September 16, 2017. The work of H. Haas was supported by the U.K. Engineering and Physical Sciences Research Council under Grant EP/K008757/1. *(Corresponding author: Harald Haas.)*

Y. Jiang is with the School of Electronics and Information Engineering, Harbin Institute of Technology, Shenzhen 518055, China (e-mail: jiangyufei@hit.edu.cn).

Y. Wang, M. Safari, J. Thompson, and H. Haas are with the Institute for Digital Communications, The University of Edinburgh, Edinburgh EH9 3JL, U.K. (e-mail: yunlu.wang@ed.ac.uk; majid.safari@ed.ac.uk; john.thompson@ed.ac.uk; h.haas@ed.ac.uk).

P. Cao is with the School of Engineering and Technology, University of Hertfordshire, U.K. (e-mail: p.cao@herts.ac.uk).

Color versions of one or more of the figures in this paper are available online at http://ieeexplore.ieee.org.

Digital Object Identifier 10.1109/JSAC.2017.2774419

Thus, it is not efficient in terms of bandwidth, compared to DCO-OFDM.

However, OFDM based systems are vulnerable to synchronization errors [7], [10]–[16]. As incoherent modulation, *i.e.*, IM/DD, is used for LiFi systems, the frequency synchronization problem of carrier frequency offset (CFO) [17] is inherently absent. Therefore, the remaining synchronization problems for optical OFDM systems are timing synchronization, *i.e.*, frame detection and sampling clock synchronization. The frame detection is to find the starting point of data frame. An inaccurate detection could cause ISI that degrades the system performance. The sampling clock synchronization is to estimate the sampling clock offset (SCO) within a sampling period. This offset is equal to the fraction of the sampling period [13], and causes inter-carrier interference (ICI) [14]–[16].

A number of frame detection methods are proposed in the literature using training sequences [10], [12], [13], [18]. In [10], Schmidl uses the correlation of repetition of codes for frame detection. However, the method in [10] suffers from shallow gradient peaks, and the frame detection is not accurate. In [12], an improved method is proposed by Park, where the starting point of data frame is detected by the strongest power at the receiver. However, this method requires cancellation of positive and negative parts in the time-domain signals, which is not possible for LiFi systems with non-negative and real signals. In [18], Park's frame detection method is modified particularity for DCO-OFDM LiFi systems. However, this method is not robust against SCO.

The sampling clock synchronization is another important issue for DCO-OFDM systems. In [13], the effect of SCO is simply analysed for ACO-OFDM systems. In [14], a resynchronization filter is proposed to compensate for the effect of SCO. In [15] and [16], sampling clock synchronization methods are proposed. However, the frame detection is not considered. To the best of our knowledge, a general timing synchronization process including frame detection and SCO estimation as well as channel estimation has not been investigated for DCO-OFDM LiFi systems.

B. Contribution

In this paper, we provide a comprehensive timing synchronization analysis for DCO-OFDM LiFi systems. Also, we propose a robust and low-complexity maximum likelihood (ML) based timing synchronization process that includes frame detection and SCO estimation as well as channel estimation, using a single training mechanism with respect to the optimization of training sequences, the selection of training sequence size and the selection of DC bias ratio. The contribution of this work can be elaborated in the following:

- First, to the best of our knowledge, this is the first work to apply ML to timing synchronization for DCO-OFDM LiFi systems. We propose a number of robust timing synchronization methods. Thus, a high-complexity two-dimensional search for frame detection and sampling clock synchronization can be divided into two low-complexity one-dimensional searches.
- Second, we propose a minimization of negative channel power (MNCP), a minimization of received signal power (MRSP) and a simplified minimization of received signal power (SMRSP) based frame detection approaches for LiFi systems, respectively. By exploring the non-negative property of LiFi systems, the MNCP frame detection is to minimize the sum power of negative channel coefficients, while the MRSP approach is to minimize the difference between the received and reconstructed signals. Both approaches allow energy efficiency, as they can perform well at low level of DC bias ratio. SMRSP, a special case of MRSP, is to minimize part of difference between the received and reconstructed signals for frame detection. The SMRSP approach provides low complexity, as fine frame detection is not required. The proposed frame detection approaches are shown to be robust against the combined effects of SCO and the low-pass characteristic of LEDs.
- Third, by using the training block the same as that for frame detection, SCO and channel estimations are performed jointly. The Cramér-Rao lower bounds (CRBs) of SCO estimation and channel estimation are derived the first time for DCO-OFDM LiFi systems. In order to minimize CRBs and improve frame detection accuracy, the training is designed with respect to the optimization of training sequences, the selection of training sequence size and the selection of DC bias ratio. Therefore, the proposed training design allows trade-offs between energy efficiency, performance, complexity and spectrum efficiency.
- Fourth, simulation results show that the proposed timing synchronization structure provides bit error rate (BER) performance close to the ideal case with perfect channel state information (CSI), no SCO and perfect frame detection. The proposed three frame detection methods significantly outperform Schmidl's method [10], [13] and Park's method [12], [13], [18] in terms of probability of false frame detection. The proposed SCO estimation and channel estimation methods can provide performance close to their CRBs, respectively.

The rest of the paper is organized as follows. The system model is presented in Section II. The optimum timing synchronization is proposed in Section III. The sub-optimum timing synchronization is proposed in Section IV. Performance analysis is described in Section V. Simulation results are presented in Section VI. Section VII draws the conclusion.

C. Notations

Throughout the paper, we use bold symbols to represent vectors/matrices, and superscripts $*$, T and H to denote the complex conjugate, transpose, and complex conjugate transpose of a vector/matrix, respectively. $\mathbf{I}_N$ and $\mathbf{1}_{N\times M}$ represent an $N \times N$ identity matrix and an $N \times M$ all-one matrix, respectively. $\mathbf{X}(a:b, u:v)$ denotes a submatrix of $\mathbf{X}$ with rows a to b and columns u to v. $\mathbf{X}(u:v)$ denotes a submatrix of $\mathbf{X}$ with all rows and columns u to v. $[\mathbf{X}]_{a,b}$ denotes entry (a, b) of matrix $\mathbf{X}$. $[\mathbf{x}]_a$ denotes entry (a) of vector $\mathbf{x}$. diag$\{\mathbf{x}\}$

represents a diagonal matrix whose diagonal elements are entries of vector $\mathbf{x}$. $||\cdot||_F^2$ is the Frobenius norm. $\mathrm{E}\{\cdot\}$ denotes the expectation. trace$\{\mathbf{X}\}$ denotes the trace of matrix $\mathbf{X}$.

II. System Model

Wireless optical communications perform best with a strong line-of-sight (LoS) channel for transmissions [19], and can be described as the combination of a diffuse channel and a LoS channel. The optical wireless channel impulse response $h_{\mathrm{LiFi}}(t)$ is written as follows [20]:

$$h_{\mathrm{LiFi}}(t) = \eta_{\mathrm{LoS}}\delta(t) + h_{\mathrm{diffuse}}(t-\Delta t), \tag{1}$$

where η_{LoS} is the LoS channel component, $\delta(t)$ is the Dirac delta function, h_{diffuse} is the diffuse channel component, and Δt is the delay between the LoS signal and the first arriving diffuse signal. The LoS channel component η_{LoS} is written as follows [21]:

$$\eta_{\mathrm{LoS}} = \begin{cases} \frac{(m+1)A_{\mathrm{rx}}}{2\pi D^2}\cos^m(\phi)\cos(\phi)T(\phi)G(\varphi), & \varphi < \Psi \\ 0, & \varphi > \Psi, \end{cases} \tag{2}$$

where $m = -\ln(2)/\ln[\cos(\phi_{1/2})]$ represents the Lambertian emission order, with $\phi_{1/2}$ denoting the half-power semi-angle of LEDs, A_{rx} is the detection area of the receiver, ϕ and φ are the light radiance angle of the transmitter and the corresponding light incidence angle of the receiver, respectively, D is the distance between transmitter and receiver, $T(\phi)$ and $G(\varphi)$ are the optical filter gain at the transmitter and concentrator gain at the receiver, respectively, and Ψ denotes the field of view (FOV) at the receiver. The diffuse channel frequency response is written as follows [21]:

$$H_{\mathrm{diffuse}}(f) = \eta_{\mathrm{diff}}\frac{e^{j2\pi f\Delta t}}{1+j\frac{f}{f_0}}, \tag{3}$$

where f_0 is the 3 dB cutoff frequency, and η_{diff} is the diffuse signal gain, expressed as follows:

$$\eta_{\mathrm{diff}} = \frac{A_{\mathrm{rx}}}{A_{\mathrm{room}}}\frac{\rho}{1-\rho}, \tag{4}$$

where A_{room} is the surface area of a room, and ρ is the average reflectivity of walls.

Another effect of LiFi systems is the limited modulation bandwidth of LED, due to the low-pass characteristic of the optical front-ends. This effect causes ISI for DCO-OFDM LiFi systems, and can be approximately modelled as follows [22]:

$$h_{\mathrm{LED}}(t) = e^{-j2\pi f_b t}, \tag{5}$$

where f_b is the cutoff bandwidth of LEDs. The equivalent channel $h(t)$ can be expressed as follows [22]–[24]:

$$h(t) = h_{\mathrm{LiFi}}(t) \otimes h_{\mathrm{LED}}(t), \tag{6}$$

where $\otimes$ denotes linear convolution. The channel impulse response in Eq. (6) is sample-spaced resulting in a number of L channel path delays as $\mathbf{h} = [h(0), h(1), \ldots, h(L-1)]^T$, with $h(l)$ denoting the l-th ($l = 0, 1, \ldots, L-1$) channel discrete-time response.

In the system, a single LED transmits M-QAM symbols to the receiver, where a number of N subcarriers are used in each DCO-OFDM block. Define $s(n)$ as the symbol on subcarrier n ($n = 0, \ldots, N-1$). Complex baseband symbols are enforced to be real, by constraining the signals to have Hermitian symmetry as $s(n) = s^*(N-n)$, $n = 1, 2, \ldots, N/2-1$. Define $\mathbf{s} \triangleq [s(0), s(1), \ldots, s(N-1)]^T$. The resulting time-domain signals matrix $\tilde{\mathbf{X}}$ can be written as follows:

$$\tilde{\mathbf{X}} = \mathbf{F}^H \mathrm{diag}\{\mathbf{s}\}\mathbf{F}(1:L), \tag{7}$$

where $\mathbf{F}$ denotes the $N \times N$ DFT matrix, with (u, v) entry $[\mathbf{F}]_{u,v} = 1/\sqrt{N}\exp(-j2\pi uv/N)$, $(u, v = 0, 1, \ldots, N-1)$. The time-domain symbol on the n-th subcarrier can also be expressed as $\tilde{x}(n) = \frac{1}{\sqrt{N}}\sum_{m=0}^{N-1} s(m)e^{\frac{j2\pi mn}{N}}$. A DC bias is added to $\tilde{x}(n)$ to ensure that most of negative signals become positive. The DC bias is calculated from $\tilde{x}(n)$, defined as follows [25]:

$$\sigma_{\mathrm{DC}} = K\sqrt{\mathrm{E}\{\tilde{x}^2(n)\}}, \tag{8}$$

where K is the DC bias ratio. By clipping the remaining negative signals, the resulting symbol $x(n)$ is written as follows:

$$x(n) = \tilde{x}(n) + \sigma_{\mathrm{DC}} + w_{\mathrm{clip}}(n), \tag{9}$$

where $w_{\mathrm{clip}}(n)$ is the clipping noise, given by

$$w_{\mathrm{clip}}(n) = \begin{cases} 0, & [\tilde{x}(n)+\sigma_{\mathrm{DC}}] > 0 \\ -\tilde{x}(n) - \sigma_{\mathrm{DC}}, & [\tilde{x}(n)+\sigma_{\mathrm{DC}}] \leqslant 0. \end{cases} \tag{10}$$

Using $\tilde{\mathbf{X}}$ in Eq. (6), the transmitted signals matrix $\mathbf{X}$ can also be written as follows:

$$\mathbf{X} = \tilde{\mathbf{X}} + \sigma_{\mathrm{DC}}\mathbf{1}_{N\times L} + \mathbf{W}_{\mathrm{clip}}, \tag{11}$$

where $\mathbf{W}_{\mathrm{clip}} \triangleq [\mathbf{w}_{\mathrm{clip}}(0), \mathbf{w}_{\mathrm{clip}}(1), \ldots, \mathbf{w}_{\mathrm{clip}}(L-1)]$, $\mathbf{w}_{\mathrm{clip}}(l) \triangleq [w_{\mathrm{clip}}(0,l), w_{\mathrm{clip}}(1,l), \ldots, w_{\mathrm{clip}}(N-1,l)]^T$. We define $\tau \in (-0.5, 0.5)$ as the SCO, normalized by symbol duration T. The received signal is oversampled by a oversampling ratio Q, and the sampling interval is $T_s = T/Q$. In order to avoid inter-block interference (IBI) caused by the channel and the low-pass characteristic of the optical front-ends as shown in Eq. (6), each DCO-OFDM block is prepended with a cyclic prefix (CP) of length $L_{\mathrm{cp}} \geq L-1$ before transmission. Assuming perfect frame detection, the oversampled signal vector $\mathbf{y} \triangleq [y(0), y(1), \ldots, y(QN-1)]^T$ for each DCO-OFDM block is written as follows [14], [16]:

$$\mathbf{y} = \mathbf{G}(\tau)\mathbf{X}\mathbf{h} + \mathbf{w}, \tag{12}$$

where $\mathbf{G}(\tau) \triangleq [\mathbf{g}(0), \mathbf{g}(1), \ldots, \mathbf{g}(N-1)]$, $\mathbf{g}(n) \triangleq [g(-nT-\tau T), g(-nT+T_s-\tau T), \ldots, g(-nT+(QN-1)T_s-\tau T)]^T$, with $g(n)$ being the pulse shaping filter; and $\mathbf{w} \triangleq [w(0), w(1), \ldots, w(QN-1)]^T$, with $w(n)$ denoting the shot and thermal noises, modelled as additive white Gaussian noise (AWGN) whose entries are independent identically distributed (i.i.d.) Gaussian random variables with zero mean and the summed variance σ^2 of short noise and thermal noise.

III. Optimum Timing Synchronization

A. Timing Error Effects

For LiFi DCO-OFDM systems, timing synchronization process consists of frame detection and sampling clock synchronization. The inaccurate frame detection leads to timing offset errors, while SCO causes ICI between subcarriers of DCO-OFDM systems.

1) Timing Offset: The equivalent channel model in Eq. (6) could cause a channel delay path of L as interference to the next block. If the length of CP is long enough, the CP contains a number of symbols that are not affected by the previous block. If the starting point of data frame is in the ISI free range, the orthogonality of subcarriers is maintained.

Let $\mathbf{I}_m = \{-L_{\text{cp}}, \ldots, 0, \ldots, N-1\}$ be the index vector of symbols in each DCO-OFDM block. Define $\epsilon = \hat{\theta}_\epsilon - \theta_\epsilon$ as the timing offset, with $\hat{\theta}_\epsilon$ and θ_ϵ denoting the estimate and real starting points of data frame, respectively.

- If $\epsilon = 0$, the starting point of data frame is the position of "$0''$ in vector $\mathbf{I}_m$, and there is no timing offset.
- If $\epsilon \in (-\infty, -L + L_{\text{cp}})$ and $\epsilon \in (0, \infty)$, ICI and inter-block interference (IBI) are generated in the received samples.
- If $\epsilon \in [-L + L_{\text{cp}}, 0)$, the symbol offset error causes a phase rotation of $\exp(j2\pi n\epsilon/N)$ on the n-th subcarrier symbol. This effect can be compensated for by channel equalization.

Therefore, the CP should be long enough to protect the inaccurate frame detection.

2) Sampling Clock Offset: The SCO has two effects: sampling clock phase offset and sampling clock frequency offset. The sampling clock phase offset causes a phase shift, the same as the phase rotation caused by timing offsets, which can also be corrected by channel equalization. The clock frequency offset causes ICI and ISI, which can degrade the system performance.

B. Problem Formulation

In this paper, we first propose an optimum joint ML timing synchronization method by a single block, performing frame detection, SCO estimation and channel estimation for DCO-OFDM systems. For frame detection, the ML is performed in the time domain using a window of size QN on the received samples to move forward or backward. At the same time, the SCO and channels can be estimated jointly alongside with frame detection.

Let $\tilde{\theta}_\epsilon$ and $\tilde{\tau}$ denote the trial index for the start position of the frame and the trial value of the SCO, respectively. Define $\mathbf{y}_{NQ}(\tilde{\theta}_\epsilon) = [y(\tilde{\theta}_\epsilon), y(1+\tilde{\theta}_\epsilon), \ldots, y(QN+\tilde{\theta}_\epsilon-1)]^T$. The optimum joint ML estimates of the start point θ_ϵ, the SCO τ, and the channel $\mathbf{h}$ are performed by addressing the cost function as follows:

$$\Lambda\left(\mathbf{y}_{NQ}(\tilde{\theta}_\epsilon); \tilde{\tau}, \tilde{\theta}_\epsilon, \mathbf{h}(\tilde{\theta}_\epsilon, \tilde{\tau})\right) = \frac{1}{(\pi\sigma^2)^{NQ}} \cdot \exp\left\{-\frac{1}{\sigma^2}\left|\left|\mathbf{y}_{NQ}(\tilde{\theta}_\epsilon) - \mathbf{G}(\tilde{\tau})\mathbf{X}\mathbf{h}(\tilde{\theta}_\epsilon, \tilde{\tau})\right|\right|_F^2\right\}, \quad (13)$$

where $\mathbf{h}(\tilde{\theta}_\epsilon, \tilde{\tau})$ is the estimate of channel with the effect of $\tilde{\theta}_\epsilon$ and $\tilde{\tau}$.

Remark 1: For OFDM RF systems with complex-valued signals, the traditional solution to Problem (13) is to maximize the equation of $\mathbf{y}_{NQ}^H(\tilde{\theta}_\epsilon)\mathbf{\Psi}\mathbf{y}_{NQ}(\tilde{\theta}_\epsilon)$ with $\mathbf{\Psi} = \mathbf{G}(\tilde{\tau})\mathbf{X}\left(\mathbf{X}^H\mathbf{G}^H(\tilde{\tau})\mathbf{G}(\tilde{\tau})\mathbf{X}\right)^{-1}\mathbf{X}^H\mathbf{G}^H(\tilde{\tau})$ [16]. However, the received signals in LiFi systems are real not complex, and unipolar not bipolar. Maximizing the RF based equation above with complex-valued signals does not provide a correct solution to Problem (13) with real-valued signals. Instead, we propose another solution by minimizing Problem (13) to perform the joint frame detection and sampling clock synchronization.

Remark 2: The optimal solution to Problem (13) leads to extremely high computational complexity, as a two-dimensional search is required for joint frame detection and sampling clock synchronization. Thus, we propose a timing synchronization structure that can reduce the high-complexity two-dimensional search to two low-complexity one-dimensional searches.

IV. Sub-Optimum Timing Synchronization

By exploring a number of properties of DCO-OFDM LiFi systems, a sub-optimum timing synchronization method is proposed, dividing the whole process into a frame detection step and a sampling clock synchronization step, as shown in Fig. 1. Thus, the high-complex two-dimensional search can be divided into two low-complexity one-dimensional searches. In this paper, all timing synchronization processes are performed using a single DCO-OFDM block, described as follows. First, a number of two coarse frame detection methods are proposed, respectively, to detect coarse timing indexes. Next, fine frame detection is used to provide an accurate start point of data frame. Furthermore, we propose a low-complexity frame detection method, requiring no fine frame detection. Then, by using the training block the same as that for frame detection, the SCO and channels are estimated jointly. Also, two CRBs are derived for the SCO estimation and the channel estimation, respectively. In order to lower CRBs and improve estimation performance, a set of training sequences is designed.

A. Frame Detection

We propose a number of three frame detection schemes designed particularly for DCO-OFDM LiFi systems: MRSP, SMRSP and MNCP. The MRSP frame detection is performed by minimizing the power between the received and reconstructed signals. SMRSP, a special case of MRSP, is to minimize part of difference between the received and reconstructed signals. This scheme provides low complexity, as fine frame detection is not required. The MNCP technique is to minimize the sum power of negative channel coefficients, by exploring the non-negativity property of LiFi channels. The proposed frame detection methods are robust against the combined effect of the SCO and the low bandwidth of phosphor-coated LEDs. Traditional RF frame detection methods [10], [12], require negative and positive parts of received signals to detect the

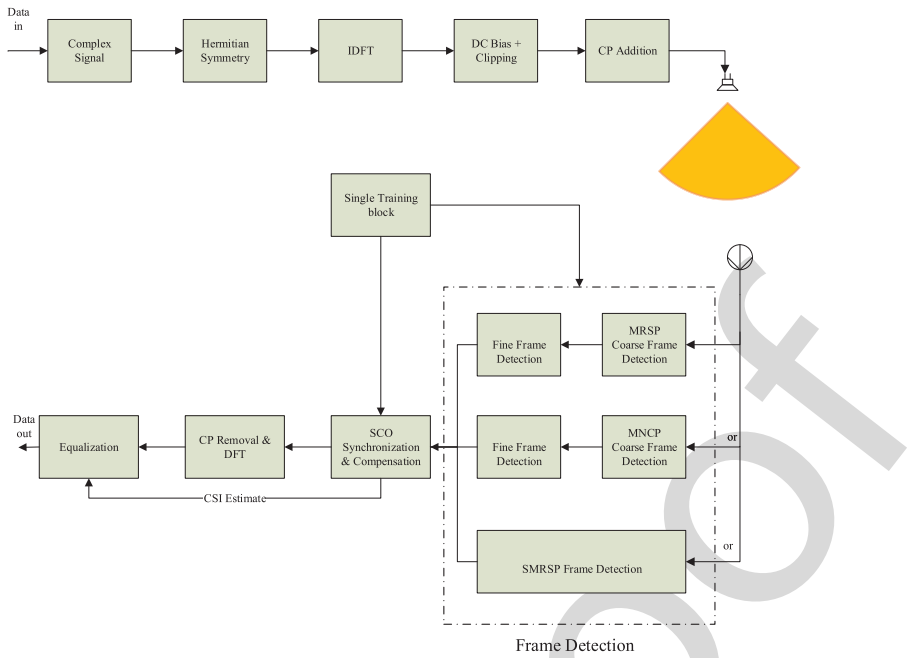

AQ:3 Fig. 1. Block diagram of the proposed timing synchronization for DCO-OFDM LiFi systems.

start point of data frame. However, the received signals in LiFi systems are real and non-negative, and are therefore not suitable for DCO-OFDM LiFi systems. Also, these methods are not robust against the SCO and the low bandwidth of phosphor-coated LEDs.

1) Coarse Frame Detection:

a) Minimization of received signal power: In order to achieve low complexity, we use a window size of N samples moving forward or backward one sample in the received signal sample vector, to search for the start point of the frame. The received signals used for detection are equivalent to extracting a symbol by every Q samples from the oversampled signals in Eq. (13) to form a received signals vector $N \times 1$ as $\mathbf{y}_N(\theta_\epsilon) = [y(Q+\theta_\epsilon), y(2Q+\theta_\epsilon), \ldots, y(QN+Q+\theta_\epsilon-1)]^T$. Since the received optical signals are positive and real, we, assuming no SCO, propose to minimize the cost function, with respect to the timing index θ_ϵ, as

$$J(\theta_\epsilon) = \left|\left|\mathbf{y}_N(\theta_\epsilon) - \mathbf{X}\mathbf{h}\right|\right|_F^2. \tag{14}$$

Define P as the length of training sequence used at the receiver. Using Eqs. (7) and (11), the training can be formulated as $\mathbf{X}_P = \tilde{\mathbf{X}}_P + \sigma_{\text{DC}}\mathbf{1}_{N\times P} + \mathbf{W}_{\text{clip}}$, with $\tilde{\mathbf{X}}_P = \mathbf{F}^H \text{diag}\{\mathbf{s}\}\mathbf{F}(1:P)$. Using the training $\mathbf{X}_P$ of size $N \times P$, the channel $\mathbf{h}(\tilde{\theta}_\epsilon)$ at the trial timing index $\tilde{\theta}_\epsilon$ is written as

$$\mathbf{h}(\tilde{\theta}_\epsilon) = \left[\mathbf{X}_P^T\mathbf{X}_P\right]^{-1}\mathbf{X}_P^T\mathbf{y}_N(\tilde{\theta}_\epsilon). \tag{15}$$

$\mathbf{h}(\tilde{\theta}_\epsilon)$ is used to reconstruct the received signal by substituting Eqs. (15) into (14). By minimizing the difference between the reconstructed signal and the received signal, the MRSP based coarse timing index $\hat{\theta}_{\epsilon_{\text{MRSP}}}$ is obtained as follows:

$$\hat{\theta}_{\epsilon_{\text{MRSP}}} = \arg\min_{\tilde{\theta}_\epsilon} \left|\left|\mathbf{y}_N(\tilde{\theta}_\epsilon) - \mathbf{X}_P\mathbf{h}(\tilde{\theta}_\epsilon)\right|\right|_F^2. \tag{16}$$

b) Simplified minimization of received signal power: When $P = 1$, the training matrix becomes a transmitted signal vector as $\mathbf{x}$. Using Eq. (15), we have

$$h(\tilde{\theta}_\epsilon) = \left(\mathbf{x}^T\mathbf{x}\right)^{-1}\mathbf{x}^T\mathbf{y}_N(\tilde{\theta}_\epsilon). \tag{17}$$

Compared with the MRSP method, SMRSP is to minimize part of difference between the received and reconstructed signals to obtain the timing index $\hat{\theta}_{\epsilon_{\text{SMRSP}}}$ by

$$\hat{\theta}_{\epsilon_{\text{SMRSP}}} = \arg\min_{\tilde{\theta}_\epsilon} \left|\left|\mathbf{y}_N(\tilde{\theta}_\epsilon) - \mathbf{x}h(\tilde{\theta}_\epsilon)\right|\right|_F^2. \tag{18}$$

Please note that SMRSP is a special case of MRSP. SMRSP is robust against the effect of the SCO and the low-pass characteristic of LEDs, requiring no fine frame detection, as the noise power is greatly reduced by the scalar of $\mathbf{x}^T\mathbf{x}$, as shown in Eq. (17).

Theorem 1: Given a fixed t in Eq. (5), higher cutoff bandwidth of the LED f_b improves the SMRSP estimation performance. When the cutoff bandwidth of LED f_b is as high as possible, MRSP becomes SMRSP.

Proof of Theorem 1: See Appendix A.

c) Minimization of negative channel power: Since the channels are unipolar and non-negative for LiFi systems, $\mathbf{h}(\tilde{\theta}_\epsilon)$ in Eq. (15) contains non-negative channel coefficients under a noiseless condition, if $\tilde{\theta}_\epsilon$ is correct, *i.e.*, $\tilde{\theta}_\epsilon = \theta_\epsilon$. When noise is present, the sum power of negative channel coefficients at the correct timing index is much lower than that at incorrect timing index, *i.e.*, $\tilde{\theta}_\epsilon \neq \theta_\epsilon$. The MNCP technique aims to minimize the sum power of the negative channel coefficients in $\mathbf{h}(\tilde{\theta}_\epsilon)$ to obtain the coarse timing index $\hat{\theta}_{\epsilon_{\text{MNCP}}}$ as follows:

$$\hat{\theta}_{\epsilon_{\text{MNCP}}} = \arg\min_{\tilde{\theta}_\epsilon} \sum_{l=0}^{P-1} \left|\left\{\left[\mathbf{h}(\tilde{\theta}_\epsilon)\right]_l < 0\right\}\right|. \tag{19}$$

B. Fine Frame Detection

The presence of SCO results in a biased coarse timing index. Therefore, further fine frame detection is required to improve the accuracy. For LiFi systems, the first received signal is the strongest LoS component [19], [20], followed by a period of no signals until the first reflected signal reaches the receiver. This is because the signal propagation delay of the LoS path is much shorter than the delay incurred by the reflected paths [19], [20]. This property is used in the fine frame detection to refine the coarse timing index. The residual timing error after coarse frame detection can be introduced into the channel, which causes the delay of the strongest path. The proposed fine frame detection method aims at finding the path delay. This can be performed by searching for the position of the strongest channel path. Plugging Eqs. (19) into (15) yields $\mathbf{h}(\hat{\theta}_{\epsilon_{\text{MNCP}}}) = \left[\mathbf{X}_P^T\mathbf{X}_P\right]^{-1}\mathbf{X}_P^T\mathbf{y}_N(\hat{\theta}_{\epsilon_{\text{MNCP}}})$. The proposed MNCP technique for fine frame detection can be described mathematically as follows:

$$\hat{\epsilon}_{\text{MNCP}} = \arg\max_{l}\left[\mathbf{h}(\hat{\theta}_{\epsilon_{\text{MNCP}}})\right]_l. \tag{20}$$

The estimated timing index $\hat{\delta}_{\text{MNCP}}$ stemming from the MNCP based method is defined as:

$$\hat{\delta}_{\text{MNCP}} = \hat{\theta}_{\epsilon_{\text{MNCP}}} + \hat{\epsilon}_{\text{MNCP}}. \tag{21}$$

Similarly, plugging Eqs. (16) into (15) yields $\mathbf{h}(\hat{\theta}_{\epsilon_{\text{MRSP}}}) = \left[\mathbf{X}_P^T\mathbf{X}_P\right]^{-1}\mathbf{X}_P^T\mathbf{y}_N(\hat{\theta}_{\epsilon_{\text{MRSP}}})$. Similar to MNCP, the delay of $\hat{\epsilon}_{\text{MRSP}}$ is obtained by searching for the position of the strongest channel path as follows:

$$\hat{\epsilon}_{\text{MRSP}} = \arg\max_{l}\left[\mathbf{h}(\hat{\theta}_{\epsilon_{\text{MRSP}}})\right]_l. \tag{22}$$

As a result and analog to Eq. (21), we obtain:

$$\hat{\delta}_{\text{MRSP}} = \hat{\theta}_{\epsilon_{\text{MRSP}}} + \hat{\epsilon}_{\text{MRSP}}. \tag{23}$$

Please note that the LoS component η_{LoS} is related to LoS channel response gain, and thus affects fine frame detection. η_{LoS} depends on the light radiance angle ϕ, and is inversely proportional to the distance D between the transmitter and receiver. When $\phi = 0$, the LoS component η_{LoS} achieves the maximum channel power at the same distance.

The SCO makes the inaccurate channel estimation in the frame detection. Thus, we need to improve channel estimation successively. In the next section, SCO and channels are considered to be jointly estimated.

C. Sampling Clock Synchronization

The training sequences that are used for frame detection can be employed again in this section to perform joint ML SCO and channel estimation. With correct timing index, the joint SCO and channel estimations are performed by minimizing the cost function as follows:

$$J(\tau, \mathbf{h}) = ||\mathbf{y} - \mathbf{G}(\tau)\mathbf{X}\mathbf{h}||_F^2. \tag{24}$$

As the SCO is between -0.5 and 0.5, we use the trial value of $\tilde{\tau}$ and the training sequences $\mathbf{X}_P$ to estimate the channel with $\tilde{\tau}$ as follows:

$$\mathbf{h}(\tilde{\tau}) = \left(\mathbf{X}_P^T\mathbf{G}^T(\tilde{\tau})\mathbf{G}(\tilde{\tau})\mathbf{X}_P\right)^{-1}\mathbf{X}_P^T\mathbf{G}^T(\tilde{\tau})\mathbf{y}. \tag{25}$$

By substituting Eqs. (25) into (24), the estimate of SCO $\hat{\tau}$ is to minimize the cost function as follows:

$$\hat{\tau} = \underset{\tilde{\tau}\in(-0.5,\,0.5)}{\arg\min}\ ||\mathbf{y} - \mathbf{G}(\tilde{\tau})\mathbf{X}_P\mathbf{h}(\tilde{\tau})||_F^2. \tag{26}$$

By substituting Eqs. (26) into (25), the channel estimation is performed as follows:

$$\hat{\mathbf{h}} = \left(\mathbf{X}_P^T\mathbf{G}^T(\hat{\tau})\mathbf{G}(\hat{\tau})\mathbf{X}_P\right)^{-1}\mathbf{X}_P^T\mathbf{G}^T(\hat{\tau})\mathbf{y}. \tag{27}$$

In a multiple input multiple output (MIMO) system, where there are multiple transmitters and receivers, Eq. (13) is still applicable. However, using Eq. (13) leads to extremely high computational complexity in the MIMO case. The proposed timing synchronization approach can divide the multi-dimensional problem into a number of one-dimensional problems, greatly reducing the complexity for MIMO systems. Therefore, the proposed approach can easily be extended to MIMO systems.

D. Cramér-Rao Lower Bound

As the SCO estimation and the channel estimation in Eqs. (26) and (27) are unbiased, CRBs [26] can be employed to provide a performance benchmark as lower bound. We derive the CRBs in terms of closed-form expression for the joint estimation of SCO τ and channel $\mathbf{h}$. As the variance of any unbiased estimator is as high as the inverse of the Fisher Information matrix, the CRB lower bound corresponds to the inverse of Fisher Information matrix. As τ and $\mathbf{h}$ are real, the estimation vector $\boldsymbol{\theta}$ can be expressed as

$$\boldsymbol{\theta} = [\tau, \mathbf{h}]^T. \tag{28}$$

Using the received signals, the corresponding Fisher Information matrix for the estimate of vector can be written as follows: [26]

$$\mathbf{F}_{\mathbf{IM}} = \frac{2}{\sigma^2}\left[\frac{\partial\mathbf{y}^T}{\partial\boldsymbol{\theta}}\frac{\partial\mathbf{y}}{\partial\boldsymbol{\theta}^T}\right]. \tag{29}$$

In the Fisher Information matrix, we should note that, 1), the diagonal elements are non-negative; and 2), the diagonal elements of the inverse of Fisher Information matrix are the bounds for the joint estimates of τ and $\mathbf{h}$. The (u, v) component of Fisher Information matrix is expressed as

$$[\mathbf{F}_{\mathbf{IM}}]_{u,v} = \frac{2}{\sigma^2}\left[\frac{\partial\mathbf{y}^T}{\partial[\boldsymbol{\theta}]_u}\frac{\partial\mathbf{y}}{\partial[\boldsymbol{\theta}]_v{}^T}\right]. \tag{30}$$

Define $\mathbf{A} = \frac{\partial\mathbf{G}(\tau)}{\partial\tau}\mathbf{X}_P$ and $\mathbf{B} = \mathbf{G}(\tau)\mathbf{X}_P$. Here, we have $\frac{\partial^2\mathbf{y}}{\partial\tau^2} = \mathbf{h}^H\mathbf{A}^H\mathbf{A}\mathbf{h}$, $\frac{\partial^2\mathbf{y}}{\partial\tau\,\partial\mathbf{h}} = \mathbf{h}^H\mathbf{A}^H\mathbf{B}$, $\frac{\partial^2\mathbf{y}}{\partial\mathbf{h}\,\partial\tau} = \mathbf{B}^H\mathbf{A}\mathbf{h}$, and $\frac{\partial^2\mathbf{y}}{\partial\mathbf{h}^2} = \mathbf{B}^H\mathbf{B}$.

The Fisher Information matrix yields:

$$\mathbf{F}_{\mathbf{IM}} = \frac{2}{\sigma^2}\begin{bmatrix}\mathbf{h}^T\mathbf{A}^T\mathbf{A}\mathbf{h} & \mathbf{h}^T\mathbf{A}^T\mathbf{B} \\ \mathbf{B}^T\mathbf{A}\mathbf{h} & \mathbf{B}^T\mathbf{B}\end{bmatrix}. \tag{31}$$

Define $\alpha = (\mathbf{h}^T\mathbf{A}^T\mathbf{\Delta_B}\mathbf{A}\mathbf{h})^{-1}$ with $\mathbf{\Delta_B} = \mathbf{I} - \mathbf{B}(\mathbf{B}^T\mathbf{B})^{-1}\mathbf{B}^T$, $\boldsymbol{\beta} = (\mathbf{B}^T\mathbf{B})^{-1}\mathbf{B}^T\mathbf{A}\mathbf{h}$, and $\mathbf{C}_h = \mathbf{B}^T\mathbf{B}$. The CRB of the joint estimation of τ and $\mathbf{h}$ is the inverse of the Fisher Information matrix, as shown in Appendix B, and this leads to:

$$\mathbf{C_{RB}} = \frac{\sigma^2}{2}\begin{bmatrix} \alpha & \alpha\boldsymbol{\beta}^T \\ \alpha\boldsymbol{\beta} & \mathbf{C}_h^{-1} + \alpha\boldsymbol{\beta}\boldsymbol{\beta}^T \end{bmatrix}. \tag{32}$$

As the diagonal elements of the $\mathbf{C_{RB}}$ matrix are corresponding to the bounds for the estimations of τ and $\mathbf{h}$, the CRB of the SCO estimation $\mathrm{C_{RB}}(\tau)$ is the $(1,1)$ entry of $\mathbf{C_{RB}}$ in Eq. (32), given as follows:

$$\begin{aligned}\mathrm{C_{RB}}(\tau) &= \frac{\sigma^2}{2}\alpha \\ &= \frac{\sigma^2}{2}\left(\mathbf{h}^T\mathbf{A}^T\mathbf{\Delta_B}\mathbf{A}\mathbf{h}\right)^{-1}.\end{aligned} \tag{33}$$

The CRB of the channel estimation $\mathbf{C_{RB}}(\mathbf{h})$ is the $(2,2)$ entry of $\mathbf{C_{RB}}$ in Eq. (32), given as follows:

$$\mathbf{C_{RB}}(\mathbf{h}) = \frac{\sigma^2}{2}\left(\mathbf{C}_h^{-1} + \alpha\boldsymbol{\beta}\boldsymbol{\beta}^H\right). \tag{34}$$

It can be observed from Eqs. (33) and (34) that the high channel gains and the strong power of training sequences can minimize the CRB of joint SCO and channel estimations.

E. Training Sequence Design

The objective of training sequence design is to minimize the CRBs with respect to the SCO and channel estimations. It is observed in Eq. (32) that $\mathbf{C_{RB}}(\mathbf{h})$ is affected by $\mathrm{C_{RB}}(\tau)$. Minimizing $\mathrm{C_{RB}}(\tau)$ corresponds to minimizing $\mathbf{C_{RB}}(\mathbf{h})$. Thus, we design a set of training sequences $\hat{\mathbf{X}}_P$ to minimize $\mathrm{C_{RB}}(\tau)$ as follows:

$$\hat{\mathbf{X}}_P = \frac{\sigma^2}{2}\arg\min_{\mathbf{X}_P}\left\{\left(\mathbf{h}^T\mathbf{A}^T\mathbf{\Delta_B}\mathbf{A}\mathbf{h}\right)^{-1}\right\}. \tag{35}$$

In other words, the optimum set of training sequences can be found by maximizing the eigenvalue of $\mathbf{h}^T\mathbf{A}^T\mathbf{\Delta_B}\mathbf{A}\mathbf{h}$. As the channel $\mathbf{h}$ is unknown, it is not possible to find a set of optimal training sequences that optimize Problem (35) with general $\mathbf{h}$. In order to make Problem (35) tractable, we can simplify Problem (35) to

$$\hat{\mathbf{X}}_P = \frac{\sigma^2}{2||\mathbf{h}||_F^2}\arg\max_{\mathbf{X}_P}\left\{\mathrm{trace}\left\{\mathbf{A}^T\mathbf{\Delta_B}\mathbf{A}\right\}\right\}. \tag{36}$$

Using Eqs. (7) and (11), $\mathbf{X}_P$ can be expressed by the frequency-domain signal $\mathbf{s}$. The optimization problem can be formulated to the design of the frequency-domain training sequences $\mathbf{s}$. Let $\mathbf{R}(\tau) = \frac{\partial\mathbf{G}(\tau)}{\partial\tau}$. Using Eq. (7) and making some arrangements, considering the effect of $\mathbf{A}^T\mathbf{A}$ in Problem (36), we can formulate the following problem to optimize training sequences as

$$\begin{aligned}\hat{\mathbf{s}} = \arg\max_{\mathbf{s}}\ &\left\{\mathrm{trace}\left\{\mathbf{F}_L^H\mathrm{diag}\{\mathbf{s}^H\}\mathbf{F}\mathbf{R}^T(\tau)\mathbf{R}(\tau)\mathbf{F}^H\mathrm{diag}\{\mathbf{s}\}\mathbf{F}_L\right\}\right\}, \\ &\text{subject to } \mathbf{s}^H\mathbf{s} = 1.\end{aligned} \tag{37}$$

We only consider the dominate and significant component $\mathbf{R}^T(\tau)\mathbf{R}(\tau)$ in (37) for the optimization of training sequences $\mathbf{s}$. We can find the solution to (37) as the eigenvector of $\mathbf{R}^T(\tau)\mathbf{R}(\tau)$ with respect to the maximum eigenvalue [27]. Define $\lambda_{\max}\{\mathbf{R}^T(\tau)\mathbf{R}(\tau)\}$ and $\mathbf{v}_{\max}\{\mathbf{R}^T(\tau)\mathbf{R}(\tau)\}$ as the largest eigenvalue and the associated eigenvector of $\mathbf{R}^T(\tau)\mathbf{R}(\tau)$, respectively. Then, we can find an optimization for Problem (37) as follows:

$$\hat{\mathbf{s}} = \mathbf{F}\mathbf{v}_{\max}\{\mathbf{R}^T(\tau)\mathbf{R}(\tau)\}. \tag{38}$$

Although the solution is not an optimal solution to the original hard coupling Problem (35). However, we provide a tractable way to establish a solution which is still meaningful in engineering applications. Note that the training sequence design depends on $\mathbf{R}^T(\tau)\mathbf{R}(\tau)$ with respect to τ which is not known in advance. However, $\mathbf{R}^T(\tau)\mathbf{R}(\tau)$ is independent of τ, with a large number of N and Q [28]. The variations of τ have no significant impact on the performance [28]. Thus, we use the range $0 - 0.1$ which sits at the center of the SCO between -0.5 and 0.5 to design the training sequences.

V. Performance Analysis

A. Complexity Analysis

For frame detection, MNCP results in (N^2P) multiplication operations, while MRSP leads to $(N^2\ P^2)$ multiplication operations. As can be seen, MNCP exhibits a P-fold complexity reduction, compared to MRSP. This is because Eq. (16) is not required in MNCP. When $P = 1$, MRSP becomes SMRSP, achieving (N^2) multiplication operations. The proposed sampling clock synchronization method requires $(N^4\ Q^3\frac{1}{\Delta})$ operations.

With each search, the proposed optimum timing synchronization in Eq. (13) needs $(N^6\ Q^3\ P^2\frac{1}{\Delta})$ operations, with Δ denoting the step size of the search for the SCO. Compared to the optimum method, the proposed sub-optimal approach can achieve a reduction of at least approximately $(N^2\ P^2)$ multiplication operations. This is equal to about $589,824$ multiplication operations reduction when $N = 64$ and $P = 12$. These parameters are used in the simulation setup in Section VI.

B. Performance Analysis for Frame Detection

1) Discussion of Training Length P: The proposed MRSP and MNCP frame detection methods can only work if the training matrix $\mathbf{X}_P$ of size $N \times P$ is singular.

- When $P = N$, $\mathbf{X}_P$ is square. Eqs. (15) and (16) are independent of $\tilde{\theta}_\epsilon$. MRSP and MNCP cannot work.
- When $P \mapsto N$, the proposed MRSP and MNCP provide worse performance, verified in Fig. 4.
- When $P \mapsto 1$, MNCP cannot perform, as sufficient training length P is required to generate the number of channel paths L, *i.e.*, $P \geq L$, as shown in Fig. 4.
- When $P = 1$, MRSP becomes SMRSP.

2) Impact of DC Bias Ratio K: When DC bias ratio K is low, all frame detection methods provide poor performance, as less optical power is used, as shown in Eq. (40). When a high level of the DC bias ratio is used, the DC power of training signals increases. The component of $(\mathbf{X}_P^T\mathbf{X}_P)^{-1}$ includes a number of stronger negative coefficients, which

TABLE I
ESTIMATORS WITH ANALYTICAL PARAMETERS (SYN.: SYNCHRONIZATION, EST.: ESTIMATION, CS: CHANNEL ESTIMATION)

Item	Frame Detection			Sampling Clock Syn.	
	MRSP	SMRSP	MNCP	SCO est.	CS
DC bias ratio K	1	2	1	5	1
Training sequence length P	1-12	1	12	6	6

is multiplied to the noise in Eq. (15) for the MNCP and MRSP techniques. The high-valued negative coefficients do not reduce the noise power. The MNCP and MRSP techniques cannot perform well. Thus, there is a careful selection of DC bias ratio, as a too low or too high level of DC bias ratio K makes the performance of the MRSP and MNCP techniques become worse. For SMRSP, the noise is reduced by the scalar of $\mathbf{x}^T\mathbf{x} \approx K^2\mathrm{E}\{\tilde{x}^2(n)\}$ as shown in Eq. (17), which is proportional to the DC bias ratio K. Thus, SMRSP provides performance improved with higher value of K used. The impact of K on a number of frame detection methods is verified in Fig. 3.

3) Discussion of Noise Reduction: The MNCP technique reduces the noise by $\left(\mathbf{X}_P^T\mathbf{X}_P\right)^{-1}\mathbf{X}_P^T$, while the MRSP technique does not reduce the noise power, as the component of $\mathbf{X}_P\left(\mathbf{X}_P^T\mathbf{X}_P\right)^{-1}\mathbf{X}_P^T$ is multiplied to the noise. For this reason, the MNCP technique provides better performance than the MRSP technique. The SMRSP frame detection reduces the noise by a scalar of $\mathbf{x}^T\mathbf{x}$. However, some negative coefficients have strong power in $(\mathbf{X}_P^T\mathbf{X}_P)^{-1}\mathbf{X}_P^T$ for the MNCP technique, which does not reduce the noise power. Thus, the SMRSP frame detection provides better performance than MNCP and MRSP techniques, verified in Fig. 2.

C. Performance Analysis for Sampling Clock Synchronization

1) Discussion of Training Length P: Let $\mathbf{B} = \mathbf{U}\mathbf{\Lambda}\mathbf{V}^T$ be the singular value decomposition (SVD), where $\mathbf{\Lambda}$ denotes the diagonal singular matrix of size $QN \times P$, $\mathbf{U}$ and $\mathbf{V}$ denote unitary matrices of sizes $QN \times QN$ and $P \times P$, respectively. Let $\tilde{\mathbf{U}} = \mathbf{U}(1 : QN, 1 : P)$. After some mathematical simplification as shown in Appendix C, Eq. (36) can be rewritten as follows:

$$\hat{\mathbf{X}}_P = \frac{\sigma^2}{2||\mathbf{h}||_F^2}\arg\max_{\mathbf{X}_P}\left\{\mathrm{trace}\left\{\mathbf{A}^T\left(\mathbf{I} - \tilde{\mathbf{U}}\tilde{\mathbf{U}}^T\right)\mathbf{A}\right\}\right\}. \quad (39)$$

$\tilde{\mathbf{U}}$ is the $QN \times P$ sub-matrix of an unitary matrix. When $P \mapsto N$, $\tilde{\mathbf{U}}\tilde{\mathbf{U}}^T$ tends towards an identity matrix, *i.e.*, $(\mathbf{I} - \tilde{\mathbf{U}}\tilde{\mathbf{U}}^T) \mapsto \mathbf{0}$. Problem (39) cannot be optimized. When $P \mapsto 1$, using Eqs. (26) and (27) does not generate a sufficient number of channel paths. Therefore, the training sequence length P should be larger than L, and much less than N. The impact of training sequence length P is verified in Fig. 7.

2) Impact of DC Bias Ratio K: Since $\mathrm{C_{RB}}(\tau)$ is a scalar, a high DC bias ratio enhances the power of training signals, and minimizes the $\mathrm{C_{RB}}(\tau)$ of the SCO estimation.

For channel estimation, the $\mathbf{C_{RB}}(\mathbf{h})$ includes $\mathbf{C}_h^{-1}$ and $\alpha\boldsymbol{\beta}\boldsymbol{\beta}^H$, as shown in Eq. (34). With a large size of $\mathbf{G}(\tau)$, it holds that $\mathbf{G}^T(\tau)\mathbf{G}(\tau) \approx \mathbf{I}$. Thus, we have $\mathbf{C}_h^{-1} \approx (\mathbf{X}_P^T\mathbf{X}_P)^{-1}$. Minimizing α, *i.e.*, $\mathrm{C_{RB}}(\tau)$, results in $||\alpha\boldsymbol{\beta}\boldsymbol{\beta}^H||_F^2 \ll ||(\mathbf{X}_P^T\mathbf{X}_P)^{-1}||_F^2$. Thus, the CRB of the channel estimation depends on the component of $\mathbf{C}_h^{-1}$ or $(\mathbf{X}_P^T\mathbf{X}_P)^{-1}$ rather than $\alpha\boldsymbol{\beta}\boldsymbol{\beta}^H$. If a low level of DC bias ratio K is used in training sequences, less optical power is used, as shown in Eq. (40). The proposed channel estimation provides poor performance. However, a high level of DC bias ratio does not minimize the CRB of the channel estimation. This is because the high DC bias makes the high power of negative coefficients in $(\mathbf{X}_P^T\mathbf{X}_P)^{-1}$, resulting in the increased value of $\mathbf{C_{RB}}(\mathbf{h})$. Thus, the DC bias ratio K should be carefully selected to trade off the SCO estimation and the channel estimation. The impact of DC bias ratio K is verified in Fig. 8.

VI. SIMULATION RESULTS

We use Monte-Carlo simulations to analyze the performance of the proposed timing synchronization methods for DCO-OFDM systems. Unless otherwise stated, the simulations assume that a data frame contains 256 DCO-OFDM blocks of $N = 64$ subcarriers. The CP length is $L_{\mathrm{CP}} = 16$. An oversampling ratio of $Q = 4$ is used. A single DCO-OFDM block is used as training, resulting in a training overhead of $1/256 = 0.39\%$. The DC bias ratio is set as $K = 1$. The training sequence length is $P = 12$ or $P = 6$. However, the optimum selection of K and P depends on method used. Table I shows the optimal selection of K and P for a number of frame detection and sampling clock synchronization methods. A raised cosine filter is employed, with roll off factor of 0.2. The symbol rates are 500 Msymbols/s. A step size of $\Delta = 0.001$ is used to search for the SCO. The training sequences are generated using SCO $\tau = 0$ or $\tau = 0.1$.

The mean squared error (MSE) between the true and estimated SCOs, is defined as $\mathrm{MSE} = \mathrm{E}\{(\tau - \hat{\tau})^2\}$. The MSE of channel estimation is defined as $\mathrm{MSE} = \mathrm{E}\{(\mathbf{h} - \hat{\mathbf{h}})^T(\mathbf{h} - \hat{\mathbf{h}})\}$. Energy per bit for optical power is denoted by $E_{b,\mathrm{opt}}$, while electrical power by $E_{b,\mathrm{ele}}$. The optical power is obtained from the electrical power as follows [8]:

$$\frac{E_{b,\mathrm{opt}}}{N_0} = \frac{K^2}{1+K^2}\frac{E_{b,\mathrm{ele}}}{N_0}. \quad (40)$$

The 3-dB cutoff bandwidth of LED is $f_b = 81.5$ MHz [19]. The room size is 5 m × 5 m × 3 m (length × width × height) [23]. The LED is located on the ceiling, with the coordinate (3 m, 3 m, 3 m). The receiver is on the desk of height 1 m facing upwards. A transmitter's light radiance angle of $\phi = 40$ degrees is used, while the receiver's corresponding light incidence angle is $\varphi = 60$ degrees [22]–[24]. The receiver detection area is $A_{\mathrm{rx}} = 1$ cm^2 is used. The half-power semi-angle of LED is $\phi_{1/2} = 60$ degrees. The average reflectivity of walls is assumed to be $\rho = 0.8$. An optical filter gain of

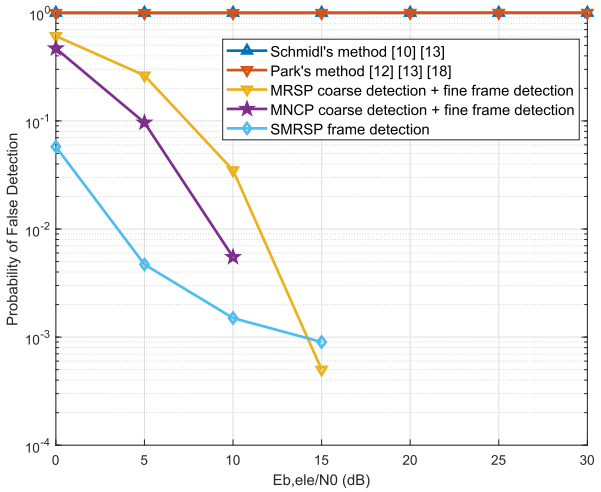

Fig. 2. Probability of false frame detection performance of the proposed MRSP, SMRSP and MNCP based frame detection methods, with $P = 12$ training sequence length and $K = 1$ DC bias ratio, in the presence of SCO.

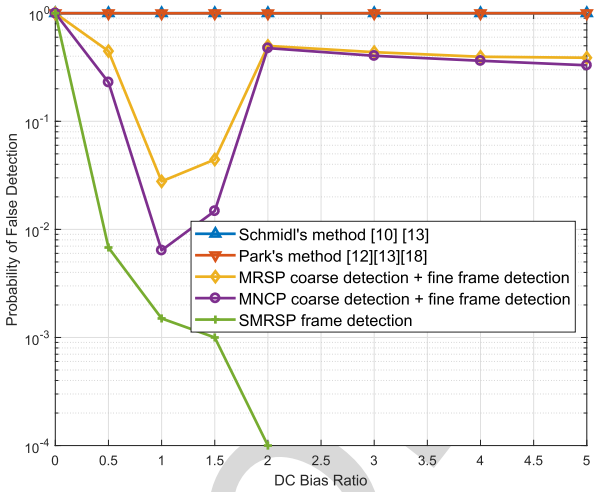

Fig. 3. Impact of DC bias ratio K on the probability of false frame detection performance of the proposed MRSP, SMRSP and MNCP based frame detection methods, with $P = 12$ training sequence length and $E_{b,\text{ele}}/N_0 = 10$ dB, in the presence of SCO.

$T(\phi) = 1$ is considered at the transmitter, while a concentrator gain of $G(\varphi) = 1$ is used at the receiver.

A. Performance of Frame Detection

In Fig. 2, the probability of false frame detection of the proposed MRSP, SMRSP and MNCP frame detection schemes is demonstrated, in comparison with Schmidl's method and Park's method [10], [12], [13], [18], in the presence of SCO. The MRSP and MNCP frame detection schemes result in performance significantly better than Schmidl's method and Park's method. MNCP outperforms MRSP in terms of 3 dB gains. This is because MNCP can reduce noise power, as discussed in Subsection V-B-3). SMRSP is robust against the effect of SCO when no fine frame detection is in place. It provides a better performance than MRSP and MNCP at low $E_{b,\text{ele}}/N_0$. This is because SMRSP can suppress noise power, more than MNCP, as discussed in Subsection V-B-3). Schmidl's and Park's methods are not robust against the combined effect of SCO and the low-pass characteristic of LED.

Fig. 3 demonstrates the impact of DC bias ratio on the false frame detection probability performance when using MRSP, SMRSP and MNCP, in the presence of SCO, with $E_{b,\text{ele}}/N_0 = 10$ dB and $P = 12$. MRSP and MNCP frame detection approaches demonstrate a concave with the variations of DC bias ratio, and achieve the best performance at $K = 1$ DC bias ratio. There is significant improvement using SMRSP when a higher DC bias ratio used. This is because the noise is reduced by the scalar of $\mathbf{x}^T\mathbf{x} \approx K^2\text{E}\{\tilde{x}^2(n)\}$, which is proportional to the DC bias ratio K, as discussed in Subsection V-B-2).

In Fig. 4, the impact of training sequence length P on the performance of false frame detection probability for the proposed methods is demonstrated, in the presence of SCO, with $E_{b,\text{ele}}/N_0 = 10$ dB and $K = 1$. SMRSP is shown with $P = 1$ training sequence length, as a special case of MRSP. With short training sequence length, MRSP provides better performance than MNCP. This is because MNCP requires

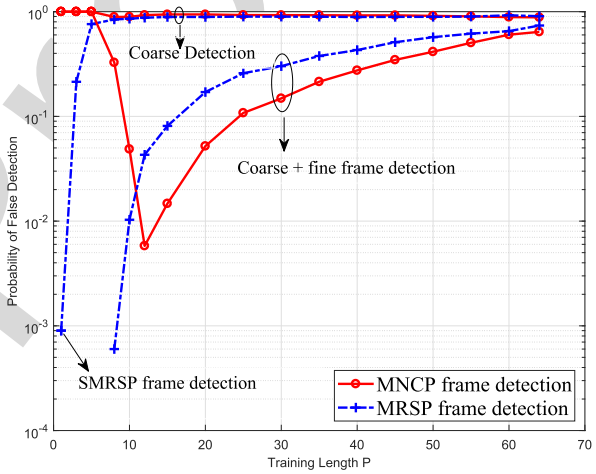

Fig. 4. Impact of training sequence length P on the probability of false frame detection performance of the proposed MRSP, SMRSP, MNCP based frame detection methods, with $K = 1$ DC bias ratio and $E_{b,\text{ele}}/N_0 = 10$ dB, in the presence of SCO.

sufficient training length to generate the total number of channel paths for frame detection. SMRSP can minimize part of difference between the received and reconstructed signals to perform frame detection. When P becomes large and close to N, the proposed methods provide worse performance, because the training matrix is close to square. This is consistent with the discussion in Subsection V-B-1).

B. Performances of Sampling Clock synchronization

Figs. 5 and 6 demonstrate the MSE performance of the proposed SCO estimation and channel estimation methods, respectively, with $K = 1$ DC bias ratio and $P = 6$ training sequence length. From $E_{b,\text{ele}}/N_0 s = 0$ dB to 15 dB, there is a big performance gap. This is due to the false frame detection, affecting the MSE performance of the proposed SCO estimation and channel estimation methods. From $E_{b,\text{ele}}/N_0 s = 15$ dB to 30 dB, the proposed SCO

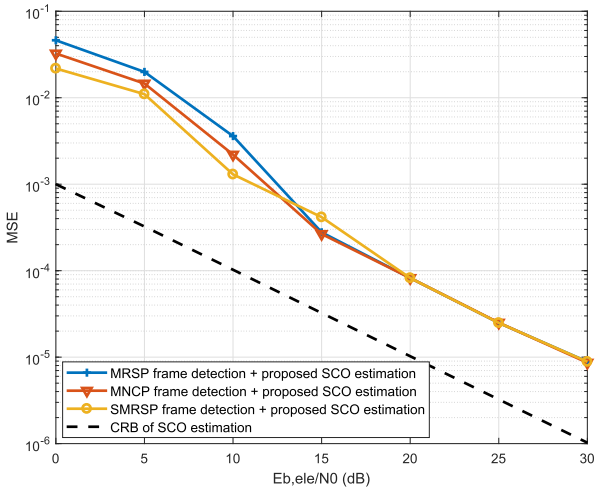

Fig. 5. MSE performance of the proposed SCO estimation, in comparison to the CRB of SCO estimation, with $K = 1$ DC bias ratio and $P = 6$ training sequence length.

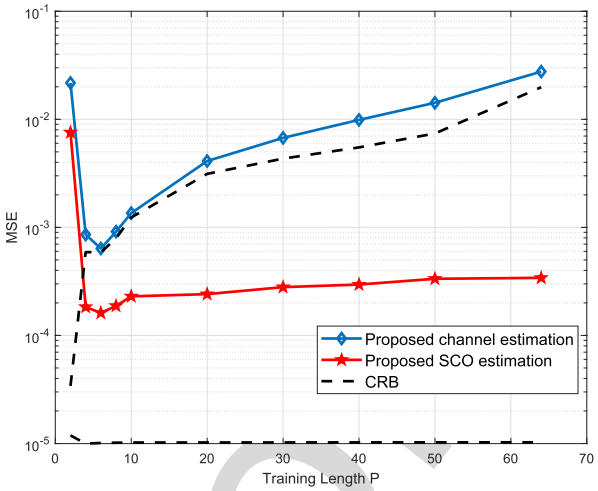

Fig. 7. Impact of the training sequence length P on the MSE performance of the proposed SCO and channel estimation methods, with $K = 1$ DC bias ratio and $E_{b,\text{ele}}/N_0 = 20$ dB.

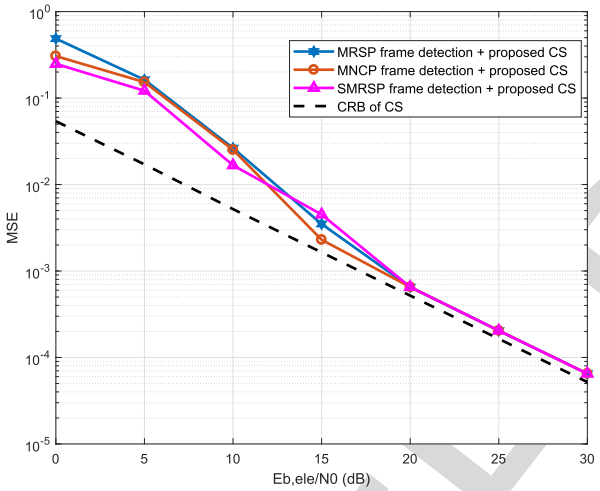

Fig. 6. MSE performance of the proposed channel estimation, in comparison to the CRB for channel estimation, with $K = 1$ DC bias ratio and $P = 6$ training sequence length. CS refers to channel estimation in the legend.

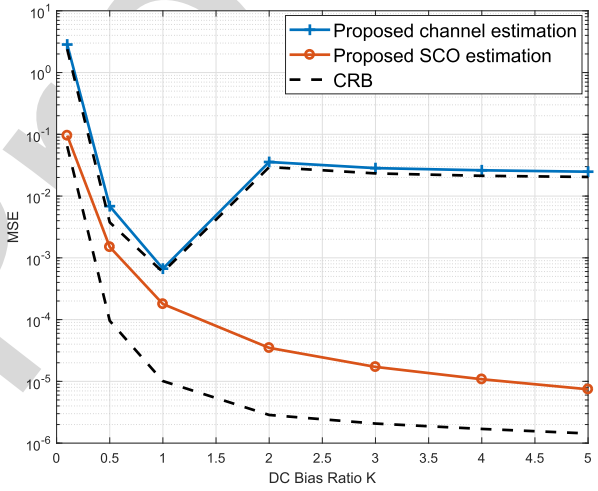

Fig. 8. Impact of the DC bias ratio K on the MSE performance of the proposed SCO and channel estimation methods, with $P = 6$ training sequence length and $E_{b,\text{ele}}/N_0 = 20$ dB.

estimation and channel estimation schemes alongside the proposed frame detection can provide MSE performance, close to their CRBs.

Fig. 7 demonstrates the impact of training sequence length P on the MSE performance of the proposed SCO and channel estimation schemes, with $E_{b,\text{ele}}/N_0 = 20$ dB and $K = 1$ DC bias ratio. The proposed SCO and channel estimation schemes show the best performance at training sequence length $P = 6$. This is because the sufficient training length P is required to generate the total number of channel paths. When P is too large, we have $(\mathbf{I} - \tilde{\mathbf{U}}\tilde{\mathbf{U}}^T) \approx \mathbf{0}$ in Eq. (39). Problem (39) cannot be optimized. The proposed SCO and channel estimation schemes cannot work. This is consistent with the discussion in Subsection V-C-1).

Fig. 8 showcases the impact of DC bias ratio K on the MSE performance of the proposed SCO and channel estimation schemes, with $E_{b,\text{ele}}/N_0 = 20$ dB and $P = 6$. The proposed SCO estimation scheme provides performance improvements when the DC bias ratio increases. This is due to two reasons: One reason is that greater optical power is used with a higher level of DC bias ratio. The other reason is that at the same time with the addition of a larger DC bias, the DC signal power can be enhanced, minimizing the $\text{C}_{\text{RB}}(\tau)$ of the SCO estimation. Thus, the proposed SCO estimation method improves. This is consistent with the discussion in Subsection V-C-2). Also, it is shown that the proposed SCO estimation scheme yield performance that is close to the CRB. For the proposed channel estimation method, a high level of DC bias ratio does not improve the performance. This is because the high DC bias makes the high power of negative coefficients in $(\mathbf{X}_P^T\mathbf{X}_P)^{-1}$, resulting in the increased value of $\mathbf{C_{RB}}(\mathbf{h})$, as discussed in Subsection V-C-2). Thus, the performance of the proposed channel estimation is shown to be concave. The best performance can be achieved at $K = 1$.

C. BER Performance of Proposed Timing Synchronization

In Fig. 9, the BER performance of the proposed timing synchronization process is demonstrated with

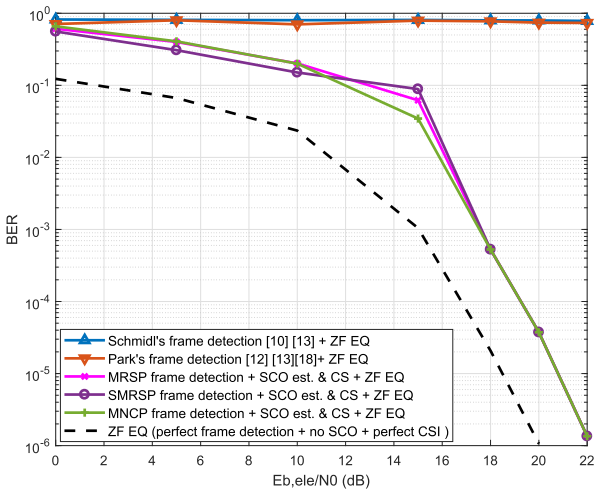

Fig. 9. BER performance of the proposed timing synchronizing scheme. EQ refers to equalization; CE refers to channel estimation and est. refers to estimation.

16 QAM modulation. The zero forcing (ZF) based equalization method with perfect frame detection, no SCO and perfect CSI is used as benchmark. The proposed timing synchronization process includes three frame detection methods, *i.e.*, MRSP, SMRSP and NMCP, and the proposed SCO and channel estimation methods. With a training overhead of 0.39%, a number of proposed timing synchronization schemes provide BER performance significantly better than Schmidl's and Park's methods [10], [12], [13], [18], and performance close to the ZF equalization based case with perfect CSI, no SCO and perfect frame detection.

VII. Conclusion

In this paper, we have proposed a timing synchronization mechanism for DCO-OFDM LiFi systems. By using a single training DCO-OFDM block, frame detection and SCO estimation can be performed together jointly with channel estimation. The proposed timing synchronization techniques provide BER performance close to the ideal case with perfect CSI, no SCO and perfect frame detection. The proposed new frame detection methods significantly outperform Schmidl's method and Park's method in terms of probability of false frame detection, and demonstrate the robustness against the SCO and the low-pass characteristic of the optical front-ends. The proposed SCO estimation and channel estimation methods result in performance close to CRBs. The proposed timing synchronization mechanism allows harnessing of trade-offs between estimation accuracy, spectral efficiency, energy efficiency, and complexity. In future work, we consider extending the timing synchronization to MIMO systems.

Appendix A
Proof of Theorem 1

Let $x(n,l)$ denote the transmitted symbol on the n-th row and l-th column of $\mathbf{X}$. Let $\mathbf{X} = [\mathbf{x}(0), \mathbf{x}(1), \ldots, \mathbf{x}(N-1)]^T$, with $\mathbf{x}(n) = [x(n,0), x(n,1), \ldots, x(n,L-1)]$. The transmitted signal vector can be written as $\mathbf{x} = [x(0,0), x(1,0), \ldots, x(N-1,0)]^T$. Eq. (17) can be re-written as follows:

$$h(\tilde{\theta}_\epsilon) = \left(\mathbf{x}^T\mathbf{x}\right)^{-1} \times \{r(0)h(0) + r(1)h(1) + \ldots r(L-1)h(L-1)\} \quad (41)$$

where $r(0) = x^2(0,0) + x^2(1,0) + \ldots + x^2(N-1,0)$, $r(1) = x(0,0)x(0,1) + \ldots x(N-1,0)x(N-1,1)$, ..., $r(L-1) = x(0,0)x(0,L-1) + \ldots x(N-1,0)x(N-1,L-1)$. Since $\mathbf{x}^T\mathbf{x} = r(0)$, the reconstructed signal in Eq. (18) is given as follows:

$$h(\tilde{\theta}_\epsilon)\mathbf{x} = h(0)\mathbf{x} + \left(\mathbf{x}^T\mathbf{x}\right)^{-1} \times \{r(1)h(1) + \ldots r(L-1)h(L-1)\}\mathbf{x}. \quad (42)$$

The first term of Eq. (42) is the part of received signals $\mathbf{y}_N(\tilde{\theta}_\epsilon)$, while the second term is the difference. The SMRSP based frame detection is to cancel the first term, by treating the second term as noise. If $f_{b_1} < f_{b_2}$, from Eq. (5), we can obtain

$$\frac{h_{\text{LED}}(t, f_{b_2})}{h_{\text{LED}}(t, f_{b_1})} = e^{j2\pi t(f_{b_1} - f_{b_2})} < 1. \quad (43)$$

We can see $h_{\text{LED}}(t, f_{b_2}) < h_{\text{LED}}(t, f_{b_1})$ with a fixed t and $t \neq 0$. Thus, the higher cutoff bandwidth leads to lower channel response of $h(1), \ldots, h(L-1)$. The power of the second term of Eq. (42) is reduced. The difference between the received and reconstructed signals is minimized. The SMRSP frame detection improves. When the cutoff bandwidth is as high as possible, we have $e^{-j2\pi f_b t} \approx 0$ with a fixed t and $t \neq 0$, resulting in $h(1), \ldots, h(L-1) \mapsto 0$. MRSP becomes SMRSP. This proves Theorem 1.

Appendix B
Mathematical Derivations of $\mathbf{C_{RB}}$

The Fisher Information matrix in Eq. (31) can be rewritten as follows:

$$\mathbf{F_{IM}} = \frac{2}{\sigma^2}\begin{bmatrix} C_\tau & \boldsymbol{\Upsilon}^T \\ \boldsymbol{\Upsilon} & \mathbf{C}_h \end{bmatrix} \quad (44)$$

where $C_\tau = \mathbf{h}^H\mathbf{A}^H\mathbf{A}\mathbf{h}$, $\mathbf{C}_h = \mathbf{B}^H\mathbf{B}$ and $\boldsymbol{\Upsilon} = \mathbf{B}^H\mathbf{A}\mathbf{h}$. According to the matrix inverse lemma [29], we can obtain the inverse of Fisher Information matrix:

$$\begin{aligned}\frac{2}{\sigma^2}\mathbf{F}_{\mathbf{IM}}^{-1} &= \begin{bmatrix} \mathbf{0}_{1\times L} \\ \mathbf{I}_{L\times L} \end{bmatrix}\mathbf{C}_h^{-1}\left[\mathbf{0}_{L\times 1}, \mathbf{I}_{L\times L}\right] \\ &\quad + \begin{bmatrix} 1 \\ -\mathbf{C}_h^{-1}\boldsymbol{\Upsilon} \end{bmatrix}\left(C_\tau - \boldsymbol{\Upsilon}^T\mathbf{C}_h^{-1}\boldsymbol{\Upsilon}\right)^{-1}\left[1 - \boldsymbol{\Upsilon}^T\mathbf{C}_h^{-1}\right] \\ &= \begin{bmatrix} 0 & \mathbf{0}_{1\times L} \\ \mathbf{0}_{L\times 1} & \mathbf{C}_h^{-1} \end{bmatrix} + \left(C_\tau - \boldsymbol{\Upsilon}^T\mathbf{C}_h^{-1}\boldsymbol{\Upsilon}\right)^{-1} \\ &\quad \times \begin{bmatrix} 1 & -\boldsymbol{\Upsilon}^T\mathbf{C}_h^{-1} \\ -\mathbf{C}_h^{-1}\boldsymbol{\Upsilon} & \mathbf{C}_h^{-1}\boldsymbol{\Upsilon}\boldsymbol{\Upsilon}^T\mathbf{C}_h^{-1} \end{bmatrix} \end{aligned} \quad (45)$$

Let $\alpha \triangleq \left(C_\tau - \boldsymbol{\Upsilon}^T\mathbf{C}_h^{-1}\boldsymbol{\Upsilon}\right)^{-1} = \left(\mathbf{h}^H\mathbf{A}^H\boldsymbol{\Delta}_\mathbf{B}\mathbf{A}\mathbf{h}\right)^{-1}$ with $\boldsymbol{\Delta}_\mathbf{B} = \mathbf{I} - \mathbf{B}(\mathbf{B}^T\mathbf{B})^{-1}\mathbf{B}^T$ and $\boldsymbol{\beta} \triangleq -\mathbf{C}_h^{-1}\boldsymbol{\Upsilon} = (\mathbf{B}^H\mathbf{B})^{-1}\mathbf{B}^H\mathbf{A}\mathbf{h}$. Eq. (45) can be rewritten:

$$\frac{2}{\sigma^2}\mathbf{F}_{\mathbf{IM}}^{-1} = \begin{bmatrix} 0 & \mathbf{0}_{1\times K} \\ \mathbf{0}_{K\times 1} & \mathbf{C}_h^{-1} \end{bmatrix} + \alpha\begin{bmatrix} 1 & \boldsymbol{\beta}^H \\ \boldsymbol{\beta} & \boldsymbol{\beta}\boldsymbol{\beta}^H \end{bmatrix}. \quad (46)$$

Thus, the joint CRB of the SCO estimation and channel estimation is expressed:

$$\mathbf{C_{RB}} = \frac{\sigma^2}{2}\begin{bmatrix} \alpha & \alpha\boldsymbol{\beta}^H \\ \alpha\boldsymbol{\beta} & \mathbf{C}_h^{-1} + \alpha\boldsymbol{\beta}\boldsymbol{\beta}^H \end{bmatrix}. \tag{47}$$

This proves Eq. (32).

Appendix C
Proof of Eq. (39)

It holds that

$$\begin{aligned}(\mathbf{B}^T\mathbf{B})^{-1} &= \left(\mathbf{V}\boldsymbol{\Lambda}^T\mathbf{U}^T \cdot \mathbf{U}\boldsymbol{\Lambda}\mathbf{V}^T\right)^{-1} = \left(\mathbf{V}\boldsymbol{\Lambda}^2\mathbf{V}^T\right)^{-1} \\ &= \mathbf{V}\boldsymbol{\Lambda}^{-2}\mathbf{V}^T. \end{aligned} \tag{48}$$

Thus,

$$\begin{aligned}\mathbf{B}(\mathbf{B}^T\mathbf{B})^{-1}\mathbf{B}^T &= \mathbf{U}\boldsymbol{\Lambda}\mathbf{V}^T \cdot \mathbf{V}\boldsymbol{\Lambda}^{-2}\mathbf{V}^T \cdot \mathbf{V}\boldsymbol{\Lambda}^T\mathbf{U}^T \\ &= \mathbf{U}\boldsymbol{\Lambda}\boldsymbol{\Lambda}^{-2}\boldsymbol{\Lambda}^T\mathbf{U}^T. \end{aligned} \tag{49}$$

Define $\tilde{\boldsymbol{\Lambda}} = \boldsymbol{\Lambda}(1:L, 1:L)$ as the diagonal matrix with diagonal elements being the eigenvalue of $\mathbf{B}$. Since $\boldsymbol{\Lambda} = [\tilde{\boldsymbol{\Lambda}}, \mathbf{0}]^T$, we have $\boldsymbol{\Lambda}^{-2} = \tilde{\boldsymbol{\Lambda}}^{-2}$ and $\boldsymbol{\Lambda}^T = [\tilde{\boldsymbol{\Lambda}}, \mathbf{0}]$. Also, we can obtain

$$\boldsymbol{\Lambda}\boldsymbol{\Lambda}^{-2}\boldsymbol{\Lambda}^T = \begin{bmatrix} \tilde{\boldsymbol{\Lambda}} \\ \mathbf{0} \end{bmatrix}\tilde{\boldsymbol{\Lambda}}^{-2}[\tilde{\boldsymbol{\Lambda}}, \mathbf{0}] = \begin{bmatrix} \mathbf{I}_{L\times L} & \mathbf{0} \\ \mathbf{0} & \mathbf{0} \end{bmatrix}. \tag{50}$$

Plugging Eq. (50) into Eq. (49) results in:

$$\begin{aligned}\boldsymbol{\Delta}_{\mathbf{B}} &= \mathbf{I} - \mathbf{B}(\mathbf{B}^T\mathbf{B})^{-1}\mathbf{B}^T \\ &= \mathbf{I} - \mathbf{U}\begin{bmatrix} \mathbf{I}_{L\times L} & \mathbf{0} \\ \mathbf{0} & \mathbf{0} \end{bmatrix}\mathbf{U}^T = \mathbf{I} - \tilde{\mathbf{U}}\tilde{\mathbf{U}}^T. \end{aligned} \tag{51}$$

This proves Eq. (39) from Eq. (36).

References

[1] Cisco, "Cisco visual networking index: Global mobile data traffic forecast update 2014–2019," Cisco, San Jose, CA, USA, White Paper, Feb. 2015.

[2] H. Burchardt, N. Serafimovski, D. Tsonev, S. Videv, and H. Haas, "VLC: Beyond point-to-point communication," *IEEE Commun. Mag.*, vol. 52, no. 7, pp. 98–105, Jul. 2014.

[3] H. Elgala, R. Mesleh, and H. Haas, "Indoor optical wireless communication: Potential and state-of-the-art," *IEEE Commun. Mag.*, vol. 49, no. 9, pp. 56–62, Sep. 2011.

[4] "Visible light communication (VLC)—A potential solution to the global wireless spectrum shortage," GBI Res., London, U.K., Tech. Rep. GBISC017MR, Mar. 2011.

[5] S. Dimitrov and H. Haas, *Principles of LED Light Communications: Towards Networked Li-Fi*. Cambridge, U.K.: Cambridge Univ. Press, 2015.

[6] K.-D. Langer *et al.*, "Optical wireless communications for broadband access in home area networks," in *Proc. 10th Anniversary Int. Conf. Trans. Opt. Netw.*, vol. 4. Jun. 2008, pp. 149–154.

[7] J. Armstrong, "OFDM for optical communications," *J. Lightw. Technol.*, vol. 27, no. 3, pp. 189–204, Feb. 1, 2009.

[8] J. Armstrong and B. Schmidt, "Comparison of asymmetrically clipped optical OFDM and DC-biased optical OFDM in AWGN," *IEEE Commun. Lett.*, vol. 12, no. 5, pp. 343–345, May 2008.

[9] D. J. F. Barros, S. K. Wilson, and J. M. Kahn, "Comparison of orthogonal frequency-division multiplexing and pulse-amplitude modulation in indoor optical wireless links," *IEEE Trans. Commun.*, vol. 60, no. 1, pp. 153–163, Jan. 2012.

[10] T. M. Schmidl and D. C. Cox, "Robust frequency and timing synchronization for OFDM," *IEEE Trans. Commun.*, vol. 45, no. 12, pp. 1613–1621, Dec. 1997.

[11] M. Speth, S. Fechtel, G. Fock, and H. Meyr, "Optimum receiver design for OFDM-based broadband transmission. II. A case study," *IEEE Trans. Wireless Commun.*, vol. 49, no. 4, pp. 571–578, Apr. 2001.

[12] B. Park, H. Cheon, C. Kang, and D. Hong, "A novel timing estimation method for OFDM systems," *IEEE Commun. Lett.*, vol. 7, no. 5, pp. 239–241, May 2003.

[13] S. Tian, K. Panta, H. A. Suraweera, B. Schmidt, S. Mclaughlin, and J. Armstrong, "A novel timing synchronization method for ACO-OFDM-based optical wireless communications," *IEEE Trans. Wireless Commun.*, vol. 7, no. 12, pp. 4958–4967, Dec. 2008.

[14] X. Li, Y. C. Wu, and E. Serpedin, "Timing synchronization in decode-and-forward cooperative communication systems," *IEEE Trans. Signal Process.*, vol. 57, no. 4, pp. 1444–1455, Apr. 2009.

[15] B. Ghimire, I. Stefan, H. Elgala, and H. Haas, "Time and frequency synchronisation in optical wireless OFDM networks," in *Proc. IEEE 22nd Int. Symp. Pers., Indoor Mobile Radio Commun.*, Sep. 2011, pp. 819–823.

[16] A. A. Nasir, H. Mehrpouyan, S. D. Blostein, S. Durrani, and R. A. Kennedy, "Timing and carrier synchronization with channel estimation in multi-relay cooperative networks," *IEEE Trans. Signal Process.*, vol. 60, no. 2, pp. 793–811, Feb. 2012.

[17] Y. Jiang, X. Zhu, E. Lim, Y. Huang, and H. Lin, "Low-complexity semiblind multi-CFO estimation and ICA-based equalization for CoMP OFDM systems," *IEEE Trans. Veh. Technol.*, vol. 63, no. 4, pp. 1928–1934, May 2014.

[18] M. F. G. Medina, O. González, S. Rodríguez, and I. R. Martín, "Timing synchronization for OFDM-based visible light communication system," in *Proc. Wireless Telecommun. Symp. (WTS)*, Apr. 2016, pp. 1–4.

[19] C. Chen, D. A. Basnayaka, and H. Haas, "Downlink performance of optical attocell networks," *J. Lightw. Technol.*, vol. 34, no. 1, pp. 137–156, Jan. 1, 2016.

[20] V. Jungnickel, V. Pohl, S. Nonnig, and C. V. Helmolt, "A physical model of the wireless infrared communication channel," *IEEE J. Sel. Areas Commun.*, vol. 20, no. 3, pp. 631–640, Apr. 2002.

[21] J. M. Kahn and J. R. Barry, "Wireless infrared communications," *Proc. IEEE*, vol. 85, no. 2, pp. 265–298, Feb. 1997.

[22] L. Zeng, D. O'Brien, H. Le-Minh, K. Lee, D. Jung, and Y. Oh, "Improvement of date rate by using equalization in an indoor visible light communication system," in *Proc. IEEE Int. Circuits Syst. Commun.*, May 2008, pp. 678–682.

[23] L. Wu, Z. Zhang, J. Dang, and H. Liu, "Adaptive modulation schemes for visible light communications," *J. Lightw. Technol.*, vol. 33, no. 1, pp. 117–125, Jan. 1, 2015.

[24] D. C. O'Brien, "Visible light communications: Challenges and potential," in *Proc. IEEE Photon. Conf.*, Oct. 2011, pp. 365–366.

[25] D. Tsonev, S. Videv, and H. Haas, "Unlocking spectral efficiency in intensity modulation and direct detection systems," *IEEE J. Sel. Areas Commun.*, vol. 33, no. 9, pp. 1758–1770, Sep. 2015.

[26] H. L. van Trees and K. L. Bell, *Bayesian Bounds for Parameter Estimation and Nonlinear Filtering/Tracking*. Hoboken, NJ, USA: Wiley, 2007.

[27] S. P. Boyd and L. Vandenberghe, *Convex Optimization*. Cambridge, U.K.: Cambridge Univ. Press, 2004.

[28] Y.-C. Wu and E. Serpedin, "Training sequences design for symbol timing estimation in MIMO correlated fading channels," in *Proc. IEEE Global Teleommun.*, Nov. 2004, pp. 81–85.

[29] T. Soderstrom and P. Stoica, *System Identification*. London, U.K.: Prentice-Hall, 1989.

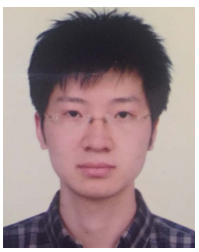

Yufei Jiang (S'12–M'14) received the Ph.D. degree from the University of Liverpool, Liverpool, U.K., in 2014. From 2014 to 2015, he was with the Department of Electrical and Electronic Engineering, University of Liverpool, as a Post-Doctoral Researcher. From 2015 to 2017, he was a Research Associate with the Institutes for Digital Communications, The University of Edinburgh, U.K. He is currently an Assistant Professor with the Harbin Institute of Technology, Shenzhen, China. His research interests include LiFi, DCO-OFDM, synchronization, full-duplex, and blind source separation.

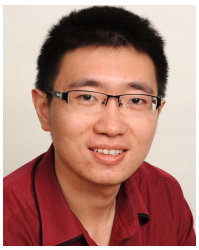

Yunlu Wang (S'14) received the B.Eng. degree in telecommunication engineering from the Beijing University of Post and Telecommunications, China, in 2011, and the double M.Sc. degrees in digital communication and signal processing from The University of Edinburgh, U.K., in 2013, and in electronic and electrical engineering from Beihang University, China, in 2014. He is currently pursuing the Ph.D. degree in electrical engineering with The University of Edinburgh. His research focus is on visible light communication and radio frequency hybrid networking.

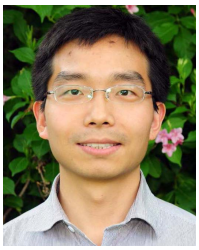

Pan Cao (S'12–M'15) received the B.Eng. degree in mechano-electronic engineering and the M.Eng. degree in information and signal processing from Xidian University, Xi'an, China, in 2008 and 2011, respectively, and the Dr.-Ing (Ph.D.) degree in electrical engineering from TU Dresden, Germany, in 2015. From 2015 to 2017, he was a Post-Doctoral Research Associate with the Institutes for Digital Communications, The University of Edinburgh, U.K., supported by the EPSRC project Seamless and Efficient Wireless Access for Future Radio Networks. He was also a Visiting Post-Doctoral Research Associate with Princeton University during the first three months of 2017. Since 2017, he has been a Senior Lecturer with the School of Engineering and Technology, University of Hertfordshire, U.K. His current research interests include millimeter-wave communication, signal processing for radar and communications, and nonconvex optimization. He received the Best Student Paper Award of the 13th IEEE International Workshop on Signal Processing Advances in Wireless Communications, Cesme, Turkey, in 2012, and the Qualcomm Innovation Fellowship Award in 2013.

Majid Safari (S'08–M'11) received the B.Sc. degree in electrical and computer engineering from the University of Tehran, Iran, in 2003, the M.Sc. degree in electrical engineering from the Sharif University of Technology, Iran, in 2005, and the Ph.D. degree in electrical and computer engineering from the University of Waterloo, Canada, in 2011. Before joining Edinburgh in 2013, he held the prestigious MITACS Elevate Strategic Fellowship at McMaster University, Canada. He is currently an Assistant Professor with the Institute for Digital Communications, The University of Edinburgh. His research interests include optical fiber and optical wireless communications, and signal processing for optical communication systems. He is currently an Associate Editor of the IEEE COMMUNICATION LETTERS. He also served as a Guest Editor of a special issue of the IEEE ACCESS journal on Optical Wireless Technologies for 5G Communications and beyond and was the TPC Co-Chair of the 4th International Workshop on Optical Wireless Communication in 2015.

John Thompson (M'94–SM'13–F'16) currently holds a Personal Chair in signal processing and communications with The University of Edinburgh, U.K. He also leads the European Marie Curie Training Network ADVANTAGE, which trains 13 Ph.D. students in Smart Grids. He has published around 300 papers in these topics and was recognized by Thomson Reuters as a Highly Cited Researcher in 2015 and 2016. His main research interests are in wireless communications, sensor signal processing, and energy-efficient communications networks and smart grids. He was a Distinguished Lecturer on green topics for ComSoc in from 2014 to 2015. He is currently an Editor of the Green Series of the *IEEE Communications Magazine* and an Associate Editor of the IEEE TRANSACTIONS ON GREEN COMMUNICATIONS AND NETWORKS.

Harald Haas received the Ph.D. degree from The University of Edinburgh in 2001, where he currently holds the Chair of mobile communications with The University of Edinburgh. He is also the Initiator, Co-Founder, and Chief Scientific Officer of pureLiFi Ltd. as well as the Director of the LiFi Research and Development Center, The University of Edinburgh. He first introduced and coined spatial modulation and LiFi. He has published 400 conference and journal papers including a paper in Science. He has co-authored a book entitled *Principles of LED Light Communications Towards Networked Li-Fi* published with Cambridge University Press in 2015. His main research interests are in optical wireless communications, hybrid optical wireless and RF communications, spatial modulation, and interference coordination in wireless networks. He was elected as a fellow of the Royal Society of Edinburgh in 2017. He was a co-recipient of recent best paper awards at VTC-Fall in 2013, VTC-Spring in 2015, ICC in 2016, and ICC in 2017. He was a co-recipient of the EURASIP Best Paper Award for the *Journal on Wireless Communications and Networking* in 2015, and a co-recipient of the Jack Neubauer Memorial Award of the IEEE Vehicular Technology Society. In 2012 and 2017, he was a recipient of the prestigious Established Career Fellowship from the Engineering and Physical Sciences Research Council (EPSRC) within Information and Communications Technology in U.K. He is an Editor of the IEEE TRANSACTIONS ON COMMUNICATIONS and the IEEE JOURNAL OF LIGHTWAVE TECHNOLOGIES. In 2014, he was selected by EPSRC as one of ten Recognizing Inspirational Scientists and Engineers Leaders in U.K. In 2016, he received the Outstanding Achievement Award from the International Solid State Lighting Alliance. LiFi was listed among the 50 best inventions in TIME Magazine 2011. He was an Invited Speaker at TED Global 2011, and his talk: Wireless Data from Every Light Bulb has been watched online more than 2.4 million times. He gave a second TED Global lecture in 2015 on the use of solar cells as LiFi data detectors and energy harvesters. This has been viewed online more than 1.8 million times.

AUTHOR QUERIES

AUTHOR PLEASE ANSWER ALL QUERIES

PLEASE NOTE: We cannot accept new source files as corrections for your paper. If possible, please annotate the PDF proof we have sent you with your corrections and upload it via the Author Gateway. Alternatively, you may send us your corrections in list format. You may also upload revised graphics via the Author Gateway.

AQ:1 = Please be advised that per instructions from the Communications Society this proof was formatted in Times Roman font and therefore some of the fonts will appear different from the fonts in your originally submitted manuscript. For instance, the math calligraphy font may appear different due to usage of the usepackage[mathcal]euscript. The Communications Society has decided not to use Computer Modern fonts in their publications.

AQ:2 = Please provide the location and postal code for "University of Hertfordshire."

AQ:3 = Note that if you require corrections/changes to tables or figures, you must supply the revised files, as these items are not edited for you.

AQ:4 = Please provide the white paper no. for ref. [1].

AQ:5 = Please provide the author names for ref. [4].

Robust and Low-Complexity Timing Synchronization for DCO-OFDM LiFi Systems

Yufei Jiang, *Member, IEEE*, Yunlu Wang, *Student Member, IEEE*, Pan Cao, *Member, IEEE*, Majid Safari, *Member, IEEE*, John Thompson, *Fellow, IEEE*, and Harald Haas, *Senior Member, IEEE*

***Abstract*— Light fidelity (LiFi), using light devices like light emitting diodes (LEDs) and visible light spectrum between 400 and 800 THz, provides a new layer of wireless connectivity within existing heterogeneous radio frequency wireless networks. Link data rates of 10 Gbps from a single transmitter have been demonstrated under ideal laboratory conditions. Synchronization is one of these issues usually assumed to be ideal. However, in a practical deployment, this is no longer a valid assumption. Therefore, we propose for the first time a low-complexity maximum likelihood-based timing synchronization process that includes frame detection and sampling clock synchronization for direct current-biased optical orthogonal frequency division multiplexing LiFi systems. The proposed timing synchronization structure can reduce the high-complexity 1-D search to two low-complexity 1-D searches for frame detection and sampling clock synchronization. By employing a single training block, frame detection can be realized, and then sampling clock offset (SCO) and channels can be estimated jointly. We propose a number of three frame detection approaches, robust against the combined effects of both SCO and the low-pass characteristic of LEDs. Furthermore, we derive the Cramér–Rao lower bounds (CRBs) of SCO and channel estimations, respectively. In order to minimize the CRBs and improve synchronization performance, a single training block is designed based on the optimization of training sequences, the selection of training length, and the selection of dc bias. Therefore, the designed training block allows us to analyze the tradeoffs between estimation accuracy, spectral efficiency, energy efficiency, and complexity. The proposed timing synchronization mechanism demonstrates low complexity and robustness benefits and provides performance significantly better than existing methods.**

***Index Terms*— Light fidelity (LiFi), sampling clock offset (SCO), frame detection, timing synchronization, DCO-OFDM.**

I. Introduction

A. Background and Motivation

THE exponentially increasing demand of mobile data traffic is saturating the spectral resources in the conventional radio frequency (RF) networks [1]–[3]. A potential solution to this spectral bottle-neck is to use high carrier frequency for wireless communications, with a large bandwidth utilized [4]. Light fidelity (LiFi) [5], which uses an extremely wide visible light spectrum for high speed communications, has recently been into the focus, and is considered as a promising technology for future networks. It has been shown in [6] that LiFi can achieve data rates up to 14 Gbps using off-the-shelf light emitting diodes (LEDs). The intensity of the light at the output of LEDs can be rapidly changed/modulated to transmit data information and to provide illumination simultaneously.

The main limitation on the data rate of LiFi systems is caused by the low bandwidth of phosphor-coated LEDs, and can cause inter-symbol interference (ISI) when using standard pulsed modulation techniques such as on-off keying (OOK). Orthogonal frequency division multiplexing (OFDM) in conjunction with bit-and-power loading [7] is an effective solution, and has also been widely used for RF systems to combat multipath fading, due to high spectrum efficiency and low-complexity channel equalization. Therefore, OFDM can be applied to solve the problem of ISI caused by LEDs for LiFi systems. OFDM allows transformation of signals between the frequency domain and the time domain by the use of inverse discrete Fourier transform (IDFT) and discrete Fourier transform (DFT). M-ary quadrature amplitude modulation (M-QAM) symbols can be mapped into a number of subcarriers for transmissions. However, complex-valued and bipolar signals are generated in the time domain, which is not applicable for intensity modulation direct detection (IM/DD) LiFi sysems, as intensity modulation optical signals are real and non-negative. This problem can partly be solved by imposing the constraint of Hermitian symmetry, resulting in real-valued signals in the time domain. However, the time-domain signals would be still negative and bipolar, which requires other techniques to make them unipolar before transmissions.

So far, there have been a number of techniques to generate unipolar OFDM signals. Direct current biased optical OFDM (DCO-OFDM) [7]–[9] is one of common techniques. A positive DC bias is introduced, and added to the time-domain signals. By clipping the negative parts of the DC biased signals, the resulting signals are non-negative and unipolar. In fact, the LED requires a level of DC bias for illumination, which can also be used to generate unipolar OFDM signals for transmissions. Asymmetrically clipped optical OFDM (ACO-OFDM) [7], [8] is another modulation technique to generate unipolar signals by clipping entire negative signals. By the appropriate selection of subcarriers, the impairment from clipping noise can be avoided. However, only a quarter of bandwidth in ACO-OFDM signals can be used to transmit data.

Manuscript February 22, 2017; July 15, 2017; September 16, 2017. The work of H. Haas was supported by the U.K. Engineering and Physical Sciences Research Council under Grant EP/K008757/1. *(Corresponding author: Harald Haas.)*

Y. Jiang is with the School of Electronics and Information Engineering, Harbin Institute of Technology, Shenzhen 518055, China (e-mail: jiangyufei@hit.edu.cn).

Y. Wang, M. Safari, J. Thompson, and H. Haas are with the Institute for Digital Communications, The University of Edinburgh, Edinburgh EH9 3JL, U.K. (e-mail: yunlu.wang@ed.ac.uk; majid.safari@ed.ac.uk; john.thompson@ed.ac.uk; h.haas@ed.ac.uk).

P. Cao is with the School of Engineering and Technology, University of Hertfordshire, U.K. (e-mail: p.cao@herts.ac.uk).

Color versions of one or more of the figures in this paper are available online at http://ieeexplore.ieee.org.

Digital Object Identifier 10.1109/JSAC.2017.2774419

Thus, it is not efficient in terms of bandwidth, compared to DCO-OFDM.

However, OFDM based systems are vulnerable to synchronization errors [7], [10]–[16]. As incoherent modulation, *i.e.*, IM/DD, is used for LiFi systems, the frequency synchronization problem of carrier frequency offset (CFO) [17] is inherently absent. Therefore, the remaining synchronization problems for optical OFDM systems are timing synchronization, *i.e.*, frame detection and sampling clock synchronization. The frame detection is to find the starting point of data frame. An inaccurate detection could cause ISI that degrades the system performance. The sampling clock synchronization is to estimate the sampling clock offset (SCO) within a sampling period. This offset is equal to the fraction of the sampling period [13], and causes inter-carrier interference (ICI) [14]–[16].

A number of frame detection methods are proposed in the literature using training sequences [10], [12], [13], [18]. In [10], Schmidl uses the correlation of repetition of codes for frame detection. However, the method in [10] suffers from shallow gradient peaks, and the frame detection is not accurate. In [12], an improved method is proposed by Park, where the starting point of data frame is detected by the strongest power at the receiver. However, this method requires cancellation of positive and negative parts in the time-domain signals, which is not possible for LiFi systems with non-negative and real signals. In [18], Park's frame detection method is modified particularity for DCO-OFDM LiFi systems. However, this method is not robust against SCO.

The sampling clock synchronization is another important issue for DCO-OFDM systems. In [13], the effect of SCO is simply analysed for ACO-OFDM systems. In [14], a resynchronization filter is proposed to compensate for the effect of SCO. In [15] and [16], sampling clock synchronization methods are proposed. However, the frame detection is not considered. To the best of our knowledge, a general timing synchronization process including frame detection and SCO estimation as well as channel estimation has not been investigated for DCO-OFDM LiFi systems.

B. Contribution

In this paper, we provide a comprehensive timing synchronization analysis for DCO-OFDM LiFi systems. Also, we propose a robust and low-complexity maximum likelihood (ML) based timing synchronization process that includes frame detection and SCO estimation as well as channel estimation, using a single training mechanism with respect to the optimization of training sequences, the selection of training sequence size and the selection of DC bias ratio. The contribution of this work can be elaborated in the following:

- First, to the best of our knowledge, this is the first work to apply ML to timing synchronization for DCO-OFDM LiFi systems. We propose a number of robust timing synchronization methods. Thus, a high-complexity two-dimensional search for frame detection and sampling clock synchronization can be divided into two low-complexity one-dimensional searches.
- Second, we propose a minimization of negative channel power (MNCP), a minimization of received signal power (MRSP) and a simplified minimization of received signal power (SMRSP) based frame detection approaches for LiFi systems, respectively. By exploring the non-negative property of LiFi systems, the MNCP frame detection is to minimize the sum power of negative channel coefficients, while the MRSP approach is to minimize the difference between the received and reconstructed signals. Both approaches allow energy efficiency, as they can perform well at low level of DC bias ratio. SMRSP, a special case of MRSP, is to minimize part of difference between the received and reconstructed signals for frame detection. The SMRSP approach provides low complexity, as fine frame detection is not required. The proposed frame detection approaches are shown to be robust against the combined effects of SCO and the low-pass characteristic of LEDs.
- Third, by using the training block the same as that for frame detection, SCO and channel estimations are performed jointly. The Cramér-Rao lower bounds (CRBs) of SCO estimation and channel estimation are derived the first time for DCO-OFDM LiFi systems. In order to minimize CRBs and improve frame detection accuracy, the training is designed with respect to the optimization of training sequences, the selection of training sequence size and the selection of DC bias ratio. Therefore, the proposed training design allows trade-offs between energy efficiency, performance, complexity and spectrum efficiency.
- Fourth, simulation results show that the proposed timing synchronization structure provides bit error rate (BER) performance close to the ideal case with perfect channel state information (CSI), no SCO and perfect frame detection. The proposed three frame detection methods significantly outperform Schmidl's method [10], [13] and Park's method [12], [13], [18] in terms of probability of false frame detection. The proposed SCO estimation and channel estimation methods can provide performance close to their CRBs, respectively.

The rest of the paper is organized as follows. The system model is presented in Section II. The optimum timing synchronization is proposed in Section III. The sub-optimum timing synchronization is proposed in Section IV. Performance analysis is described in Section V. Simulation results are presented in Section VI. Section VII draws the conclusion.

C. Notations

Throughout the paper, we use bold symbols to represent vectors/matrices, and superscripts $*$, T and H to denote the complex conjugate, transpose, and complex conjugate transpose of a vector/matrix, respectively. $\mathbf{I}_N$ and $\mathbf{1}_{N\times M}$ represent an $N \times N$ identity matrix and an $N \times M$ all-one matrix, respectively. $\mathbf{X}(a:b, u:v)$ denotes a submatrix of $\mathbf{X}$ with rows a to b and columns u to v. $\mathbf{X}(u:v)$ denotes a submatrix of $\mathbf{X}$ with all rows and columns u to v. $[\mathbf{X}]_{a,b}$ denotes entry (a, b) of matrix $\mathbf{X}$. $[\mathbf{x}]_a$ denotes entry (a) of vector $\mathbf{x}$. diag$\{\mathbf{x}\}$

represents a diagonal matrix whose diagonal elements are entries of vector $\mathbf{x}$. $||\cdot||_F^2$ is the Frobenius norm. $\mathrm{E}\{\cdot\}$ denotes the expectation. trace$\{\mathbf{X}\}$ denotes the trace of matrix $\mathbf{X}$.

II. System Model

Wireless optical communications perform best with a strong line-of-sight (LoS) channel for transmissions [19], and can be described as the combination of a diffuse channel and a LoS channel. The optical wireless channel impulse response $h_{\mathrm{LiFi}}(t)$ is written as follows [20]:

$$h_{\mathrm{LiFi}}(t) = \eta_{\mathrm{LoS}}\delta(t) + h_{\mathrm{diffuse}}(t-\Delta t), \tag{1}$$

where η_{LoS} is the LoS channel component, $\delta(t)$ is the Dirac delta function, h_{diffuse} is the diffuse channel component, and Δt is the delay between the LoS signal and the first arriving diffuse signal. The LoS channel component η_{LoS} is written as follows [21]:

$$\eta_{\mathrm{LoS}} = \begin{cases} \frac{(m+1)A_{\mathrm{rx}}}{2\pi D^2}\cos^m(\phi)\cos(\phi)T(\phi)G(\varphi), & \varphi < \Psi \\ 0, & \varphi > \Psi, \end{cases} \tag{2}$$

where $m = -\ln(2)/\ln[\cos(\phi_{1/2})]$ represents the Lambertian emission order, with $\phi_{1/2}$ denoting the half-power semi-angle of LEDs, A_{rx} is the detection area of the receiver, ϕ and φ are the light radiance angle of the transmitter and the corresponding light incidence angle of the receiver, respectively, D is the distance between transmitter and receiver, $T(\phi)$ and $G(\varphi)$ are the optical filter gain at the transmitter and concentrator gain at the receiver, respectively, and Ψ denotes the field of view (FOV) at the receiver. The diffuse channel frequency response is written as follows [21]:

$$H_{\mathrm{diffuse}}(f) = \eta_{\mathrm{diff}}\frac{e^{j2\pi f\Delta t}}{1+j\frac{f}{f_0}}, \tag{3}$$

where f_0 is the 3 dB cutoff frequency, and η_{diff} is the diffuse signal gain, expressed as follows:

$$\eta_{\mathrm{diff}} = \frac{A_{\mathrm{rx}}}{A_{\mathrm{room}}}\frac{\rho}{1-\rho}, \tag{4}$$

where A_{room} is the surface area of a room, and ρ is the average reflectivity of walls.

Another effect of LiFi systems is the limited modulation bandwidth of LED, due to the low-pass characteristic of the optical front-ends. This effect causes ISI for DCO-OFDM LiFi systems, and can be approximately modelled as follows [22]:

$$h_{\mathrm{LED}}(t) = e^{-j2\pi f_b t}, \tag{5}$$

where f_b is the cutoff bandwidth of LEDs. The equivalent channel $h(t)$ can be expressed as follows [22]–[24]:

$$h(t) = h_{\mathrm{LiFi}}(t) \otimes h_{\mathrm{LED}}(t), \tag{6}$$

where $\otimes$ denotes linear convolution. The channel impulse response in Eq. (6) is sample-spaced resulting in a number of L channel path delays as $\mathbf{h} = [h(0), h(1), \ldots, h(L-1)]^T$, with $h(l)$ denoting the l-th ($l = 0, 1, \ldots, L-1$) channel discrete-time response.

In the system, a single LED transmits M-QAM symbols to the receiver, where a number of N subcarriers are used in each DCO-OFDM block. Define $s(n)$ as the symbol on subcarrier n ($n = 0, \ldots, N-1$). Complex baseband symbols are enforced to be real, by constraining the signals to have Hermitian symmetry as $s(n) = s^*(N-n)$, $n = 1, 2, \ldots, N/2-1$. Define $\mathbf{s} \triangleq [s(0), s(1), \ldots, s(N-1)]^T$. The resulting time-domain signals matrix $\tilde{\mathbf{X}}$ can be written as follows:

$$\tilde{\mathbf{X}} = \mathbf{F}^H \mathrm{diag}\{\mathbf{s}\}\mathbf{F}(1:L), \tag{7}$$

where $\mathbf{F}$ denotes the $N \times N$ DFT matrix, with (u, v) entry $[\mathbf{F}]_{u,v} = 1/\sqrt{N}\exp(-j2\pi uv/N)$, $(u, v = 0, 1, \ldots, N-1)$. The time-domain symbol on the n-th subcarrier can also be expressed as $\tilde{x}(n) = \frac{1}{\sqrt{N}}\sum_{m=0}^{N-1} s(m)e^{\frac{j2\pi mn}{N}}$. A DC bias is added to $\tilde{x}(n)$ to ensure that most of negative signals become positive. The DC bias is calculated from $\tilde{x}(n)$, defined as follows [25]:

$$\sigma_{\mathrm{DC}} = K\sqrt{\mathrm{E}\{\tilde{x}^2(n)\}}, \tag{8}$$

where K is the DC bias ratio. By clipping the remaining negative signals, the resulting symbol $x(n)$ is written as follows:

$$x(n) = \tilde{x}(n) + \sigma_{\mathrm{DC}} + w_{\mathrm{clip}}(n), \tag{9}$$

where $w_{\mathrm{clip}}(n)$ is the clipping noise, given by

$$w_{\mathrm{clip}}(n) = \begin{cases} 0, & [\tilde{x}(n)+\sigma_{\mathrm{DC}}] > 0 \\ -\tilde{x}(n) - \sigma_{\mathrm{DC}}, & [\tilde{x}(n)+\sigma_{\mathrm{DC}}] \leqslant 0. \end{cases} \tag{10}$$

Using $\tilde{\mathbf{X}}$ in Eq. (6), the transmitted signals matrix $\mathbf{X}$ can also be written as follows:

$$\mathbf{X} = \tilde{\mathbf{X}} + \sigma_{\mathrm{DC}}\mathbf{1}_{N\times L} + \mathbf{W}_{\mathrm{clip}}, \tag{11}$$

where $\mathbf{W}_{\mathrm{clip}} \triangleq [\mathbf{w}_{\mathrm{clip}}(0), \mathbf{w}_{\mathrm{clip}}(1), \ldots, \mathbf{w}_{\mathrm{clip}}(L-1)]$, $\mathbf{w}_{\mathrm{clip}}(l) \triangleq [w_{\mathrm{clip}}(0,l), w_{\mathrm{clip}}(1,l), \ldots, w_{\mathrm{clip}}(N-1,l)]^T$. We define $\tau \in (-0.5, 0.5)$ as the SCO, normalized by symbol duration T. The received signal is oversampled by a oversampling ratio Q, and the sampling interval is $T_s = T/Q$. In order to avoid inter-block interference (IBI) caused by the channel and the low-pass characteristic of the optical front-ends as shown in Eq. (6), each DCO-OFDM block is prepended with a cyclic prefix (CP) of length $L_{\mathrm{cp}} \geq L-1$ before transmission. Assuming perfect frame detection, the oversampled signal vector $\mathbf{y} \triangleq [y(0), y(1), \ldots, y(QN-1)]^T$ for each DCO-OFDM block is written as follows [14], [16]:

$$\mathbf{y} = \mathbf{G}(\tau)\mathbf{X}\mathbf{h} + \mathbf{w}, \tag{12}$$

where $\mathbf{G}(\tau) \triangleq [\mathbf{g}(0), \mathbf{g}(1), \ldots, \mathbf{g}(N-1)]$, $\mathbf{g}(n) \triangleq [g(-nT-\tau T), g(-nT+T_s-\tau T), \ldots, g(-nT+(QN-1)T_s-\tau T)]^T$, with $g(n)$ being the pulse shaping filter; and $\mathbf{w} \triangleq [w(0), w(1), \ldots, w(QN-1)]^T$, with $w(n)$ denoting the shot and thermal noises, modelled as additive white Gaussian noise (AWGN) whose entries are independent identically distributed (i.i.d.) Gaussian random variables with zero mean and the summed variance σ^2 of short noise and thermal noise.

III. Optimum Timing Synchronization

A. Timing Error Effects

For LiFi DCO-OFDM systems, timing synchronization process consists of frame detection and sampling clock synchronization. The inaccurate frame detection leads to timing offset errors, while SCO causes ICI between subcarriers of DCO-OFDM systems.

1) Timing Offset: The equivalent channel model in Eq. (6) could cause a channel delay path of L as interference to the next block. If the length of CP is long enough, the CP contains a number of symbols that are not affected by the previous block. If the starting point of data frame is in the ISI free range, the orthogonality of subcarriers is maintained.

Let $\mathbf{I}_m = \{-L_{\text{cp}}, \ldots, 0, \ldots, N-1\}$ be the index vector of symbols in each DCO-OFDM block. Define $\epsilon = \hat{\theta}_\epsilon - \theta_\epsilon$ as the timing offset, with $\hat{\theta}_\epsilon$ and θ_ϵ denoting the estimate and real starting points of data frame, respectively.

- If $\epsilon = 0$, the starting point of data frame is the position of "0″ in vector $\mathbf{I}_m$, and there is no timing offset.
- If $\epsilon \in (-\infty, -L + L_{\text{cp}})$ and $\epsilon \in (0, \infty)$, ICI and inter-block interference (IBI) are generated in the received samples.
- If $\epsilon \in [-L + L_{\text{cp}}, 0)$, the symbol offset error causes a phase rotation of $\exp(j2\pi n\epsilon/N)$ on the n-th subcarrier symbol. This effect can be compensated for by channel equalization.

Therefore, the CP should be long enough to protect the inaccurate frame detection.

2) Sampling Clock Offset: The SCO has two effects: sampling clock phase offset and sampling clock frequency offset. The sampling clock phase offset causes a phase shift, the same as the phase rotation caused by timing offsets, which can also be corrected by channel equalization. The clock frequency offset causes ICI and ISI, which can degrade the system performance.

B. Problem Formulation

In this paper, we first propose an optimum joint ML timing synchronization method by a single block, performing frame detection, SCO estimation and channel estimation for DCO-OFDM systems. For frame detection, the ML is performed in the time domain using a window of size QN on the received samples to move forward or backward. At the same time, the SCO and channels can be estimated jointly alongside with frame detection.

Let $\tilde{\theta}_\epsilon$ and $\tilde{\tau}$ denote the trial index for the start position of the frame and the trial value of the SCO, respectively. Define $\mathbf{y}_{NQ}(\tilde{\theta}_\epsilon) = [y(\tilde{\theta}_\epsilon), y(1+\tilde{\theta}_\epsilon), \ldots, y(QN+\tilde{\theta}_\epsilon-1)]^T$. The optimum joint ML estimates of the start point θ_ϵ, the SCO τ, and the channel $\mathbf{h}$ are performed by addressing the cost function as follows:

$$\Lambda\left(\mathbf{y}_{NQ}(\tilde{\theta}_\epsilon); \tilde{\tau}, \tilde{\theta}_\epsilon, \mathbf{h}(\tilde{\theta}_\epsilon, \tilde{\tau})\right) = \frac{1}{(\pi\sigma^2)^{NQ}} \cdot \exp\left\{-\frac{1}{\sigma^2}\left|\left|\mathbf{y}_{NQ}(\tilde{\theta}_\epsilon) - \mathbf{G}(\tilde{\tau})\mathbf{X}\mathbf{h}(\tilde{\theta}_\epsilon, \tilde{\tau})\right|\right|_F^2\right\}, \quad (13)$$

where $\mathbf{h}(\tilde{\theta}_\epsilon, \tilde{\tau})$ is the estimate of channel with the effect of $\tilde{\theta}_\epsilon$ and $\tilde{\tau}$.

Remark 1: For OFDM RF systems with complex-valued signals, the traditional solution to Problem (13) is to maximize the equation of $\mathbf{y}_{NQ}^H(\tilde{\theta}_\epsilon)\mathbf{\Psi}\mathbf{y}_{NQ}(\tilde{\theta}_\epsilon)$ with $\mathbf{\Psi} = \mathbf{G}(\tilde{\tau})\mathbf{X}\left(\mathbf{X}^H\mathbf{G}^H(\tilde{\tau})\mathbf{G}(\tilde{\tau})\mathbf{X}\right)^{-1}\mathbf{X}^H\mathbf{G}^H(\tilde{\tau})$ [16]. However, the received signals in LiFi systems are real not complex, and unipolar not bipolar. Maximizing the RF based equation above with complex-valued signals does not provide a correct solution to Problem (13) with real-valued signals. Instead, we propose another solution by minimizing Problem (13) to perform the joint frame detection and sampling clock synchronization.

Remark 2: The optimal solution to Problem (13) leads to extremely high computational complexity, as a two-dimensional search is required for joint frame detection and sampling clock synchronization. Thus, we propose a timing synchronization structure that can reduce the high-complexity two-dimensional search to two low-complexity one-dimensional searches.

IV. Sub-Optimum Timing Synchronization

By exploring a number of properties of DCO-OFDM LiFi systems, a sub-optimum timing synchronization method is proposed, dividing the whole process into a frame detection step and a sampling clock synchronization step, as shown in Fig. 1. Thus, the high-complex two-dimensional search can be divided into two low-complexity one-dimensional searches. In this paper, all timing synchronization processes are performed using a single DCO-OFDM block, described as follows. First, a number of two coarse frame detection methods are proposed, respectively, to detect coarse timing indexes. Next, fine frame detection is used to provide an accurate start point of data frame. Furthermore, we propose a low-complexity frame detection method, requiring no fine frame detection. Then, by using the training block the same as that for frame detection, the SCO and channels are estimated jointly. Also, two CRBs are derived for the SCO estimation and the channel estimation, respectively. In order to lower CRBs and improve estimation performance, a set of training sequences is designed.

A. Frame Detection

We propose a number of three frame detection schemes designed particularly for DCO-OFDM LiFi systems: MRSP, SMRSP and MNCP. The MRSP frame detection is performed by minimizing the power between the received and reconstructed signals. SMRSP, a special case of MRSP, is to minimize part of difference between the received and reconstructed signals. This scheme provides low complexity, as fine frame detection is not required. The MNCP technique is to minimize the sum power of negative channel coefficients, by exploring the non-negativity property of LiFi channels. The proposed frame detection methods are robust against the combined effect of the SCO and the low bandwidth of phosphor-coated LEDs. Traditional RF frame detection methods [10], [12], require negative and positive parts of received signals to detect the

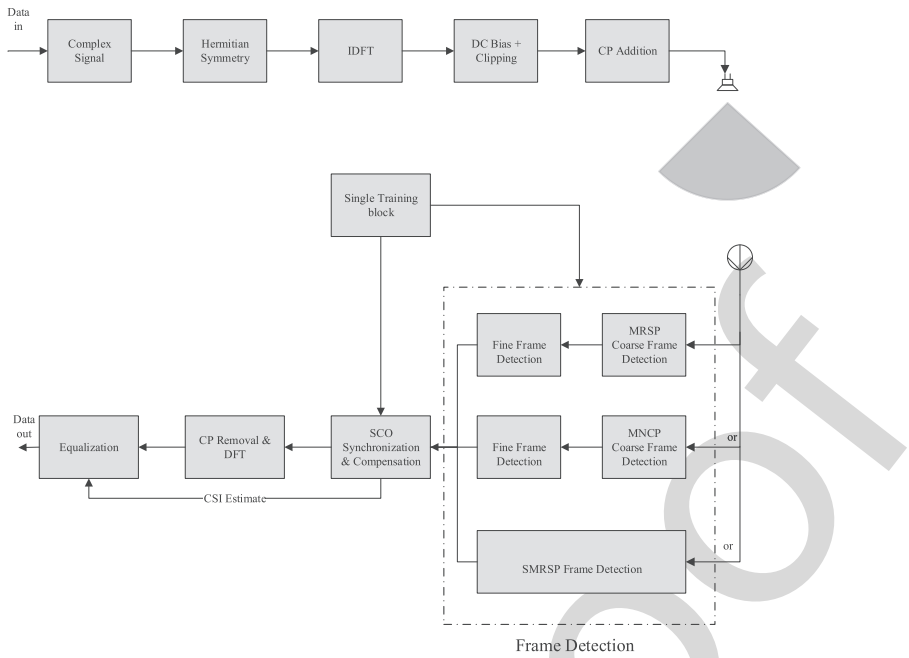

AQ:3 Fig. 1. Block diagram of the proposed timing synchronization for DCO-OFDM LiFi systems.

start point of data frame. However, the received signals in LiFi systems are real and non-negative, and are therefore not suitable for DCO-OFDM LiFi systems. Also, these methods are not robust against the SCO and the low bandwidth of phosphor-coated LEDs.

1) Coarse Frame Detection:

a) Minimization of received signal power: In order to achieve low complexity, we use a window size of N samples moving forward or backward one sample in the received signal sample vector, to search for the start point of the frame. The received signals used for detection are equivalent to extracting a symbol by every Q samples from the oversampled signals in Eq. (13) to form a received signals vector $N \times 1$ as $\mathbf{y}_N(\theta_\epsilon) = [y(Q+\theta_\epsilon), y(2Q+\theta_\epsilon), \ldots, y(QN+Q+\theta_\epsilon-1)]^T$. Since the received optical signals are positive and real, we, assuming no SCO, propose to minimize the cost function, with respect to the timing index θ_ϵ, as

$$J(\theta_\epsilon) = \left|\left|\mathbf{y}_N(\theta_\epsilon) - \mathbf{X}\mathbf{h}\right|\right|_F^2. \tag{14}$$

Define P as the length of training sequence used at the receiver. Using Eqs. (7) and (11), the training can be formulated as $\mathbf{X}_P = \tilde{\mathbf{X}}_P + \sigma_{\text{DC}}\mathbf{1}_{N\times P} + \mathbf{W}_{\text{clip}}$, with $\tilde{\mathbf{X}}_P = \mathbf{F}^H \text{diag}\{\mathbf{s}\}\mathbf{F}(1:P)$. Using the training $\mathbf{X}_P$ of size $N \times P$, the channel $\mathbf{h}(\tilde{\theta}_\epsilon)$ at the trial timing index $\tilde{\theta}_\epsilon$ is written as

$$\mathbf{h}(\tilde{\theta}_\epsilon) = \left[\mathbf{X}_P^T\mathbf{X}_P\right]^{-1}\mathbf{X}_P^T\mathbf{y}_N(\tilde{\theta}_\epsilon). \tag{15}$$

$\mathbf{h}(\tilde{\theta}_\epsilon)$ is used to reconstruct the received signal by substituting Eqs. (15) into (14). By minimizing the difference between the reconstructed signal and the received signal, the MRSP based coarse timing index $\hat{\theta}_{\epsilon_{\text{MRSP}}}$ is obtained as follows:

$$\hat{\theta}_{\epsilon_{\text{MRSP}}} = \arg\min_{\tilde{\theta}_\epsilon} \left|\left|\mathbf{y}_N(\tilde{\theta}_\epsilon) - \mathbf{X}_P\mathbf{h}(\tilde{\theta}_\epsilon)\right|\right|_F^2. \tag{16}$$

b) Simplified minimization of received signal power: When $P = 1$, the training matrix becomes a transmitted signal vector as $\mathbf{x}$. Using Eq. (15), we have

$$h(\tilde{\theta}_\epsilon) = \left(\mathbf{x}^T\mathbf{x}\right)^{-1}\mathbf{x}^T\mathbf{y}_N(\tilde{\theta}_\epsilon). \tag{17}$$

Compared with the MRSP method, SMRSP is to minimize part of difference between the received and reconstructed signals to obtain the timing index $\hat{\theta}_{\epsilon_{\text{SMRSP}}}$ by

$$\hat{\theta}_{\epsilon_{\text{SMRSP}}} = \arg\min_{\tilde{\theta}_\epsilon} \left|\left|\mathbf{y}_N(\tilde{\theta}_\epsilon) - \mathbf{x}h(\tilde{\theta}_\epsilon)\right|\right|_F^2. \tag{18}$$

Please note that SMRSP is a special case of MRSP. SMRSP is robust against the effect of the SCO and the low-pass characteristic of LEDs, requiring no fine frame detection, as the noise power is greatly reduced by the scalar of $\mathbf{x}^T\mathbf{x}$, as shown in Eq. (17).

Theorem 1: Given a fixed t in Eq. (5), higher cutoff bandwidth of the LED f_b improves the SMRSP estimation performance. When the cutoff bandwidth of LED f_b is as high as possible, MRSP becomes SMRSP.

Proof of Theorem 1: See Appendix A.

c) Minimization of negative channel power: Since the channels are unipolar and non-negative for LiFi systems, $\mathbf{h}(\tilde{\theta}_\epsilon)$ in Eq. (15) contains non-negative channel coefficients under a noiseless condition, if $\tilde{\theta}_\epsilon$ is correct, *i.e.*, $\tilde{\theta}_\epsilon = \theta_\epsilon$. When noise is present, the sum power of negative channel coefficients at the correct timing index is much lower than that at incorrect timing index, *i.e.*, $\tilde{\theta}_\epsilon \neq \theta_\epsilon$. The MNCP technique aims to minimize the sum power of the negative channel coefficients in $\mathbf{h}(\tilde{\theta}_\epsilon)$ to obtain the coarse timing index $\hat{\theta}_{\epsilon_{\text{MNCP}}}$ as follows:

$$\hat{\theta}_{\epsilon_{\text{MNCP}}} = \arg\min_{\tilde{\theta}_\epsilon} \sum_{l=0}^{P-1} \left|\left\{\left[\mathbf{h}(\tilde{\theta}_\epsilon)\right]_l < 0\right\}\right|. \tag{19}$$

B. Fine Frame Detection

The presence of SCO results in a biased coarse timing index. Therefore, further fine frame detection is required to improve the accuracy. For LiFi systems, the first received signal is the strongest LoS component [19], [20], followed by a period of no signals until the first reflected signal reaches the receiver. This is because the signal propagation delay of the LoS path is much shorter than the delay incurred by the reflected paths [19], [20]. This property is used in the fine frame detection to refine the coarse timing index. The residual timing error after coarse frame detection can be introduced into the channel, which causes the delay of the strongest path. The proposed fine frame detection method aims at finding the path delay. This can be performed by searching for the position of the strongest channel path. Plugging Eqs. (19) into (15) yields $\mathbf{h}(\hat{\theta}_{\epsilon_{\text{MNCP}}}) = \left[\mathbf{X}_P^T\mathbf{X}_P\right]^{-1}\mathbf{X}_P^T\mathbf{y}_N(\hat{\theta}_{\epsilon_{\text{MNCP}}})$. The proposed MNCP technique for fine frame detection can be described mathematically as follows:

$$\hat{\epsilon}_{\text{MNCP}} = \arg\max_{l}\left[\mathbf{h}(\hat{\theta}_{\epsilon_{\text{MNCP}}})\right]_l. \tag{20}$$

The estimated timing index $\hat{\delta}_{\text{MNCP}}$ stemming from the MNCP based method is defined as:

$$\hat{\delta}_{\text{MNCP}} = \hat{\theta}_{\epsilon_{\text{MNCP}}} + \hat{\epsilon}_{\text{MNCP}}. \tag{21}$$

Similarly, plugging Eqs. (16) into (15) yields $\mathbf{h}(\hat{\theta}_{\epsilon_{\text{MRSP}}}) = \left[\mathbf{X}_P^T\mathbf{X}_P\right]^{-1}\mathbf{X}_P^T\mathbf{y}_N(\hat{\theta}_{\epsilon_{\text{MRSP}}})$. Similar to MNCP, the delay of $\hat{\epsilon}_{\text{MRSP}}$ is obtained by searching for the position of the strongest channel path as follows:

$$\hat{\epsilon}_{\text{MRSP}} = \arg\max_{l}\left[\mathbf{h}(\hat{\theta}_{\epsilon_{\text{MRSP}}})\right]_l. \tag{22}$$

As a result and analog to Eq. (21), we obtain:

$$\hat{\delta}_{\text{MRSP}} = \hat{\theta}_{\epsilon_{\text{MRSP}}} + \hat{\epsilon}_{\text{MRSP}}. \tag{23}$$

Please note that the LoS component η_{LoS} is related to LoS channel response gain, and thus affects fine frame detection. η_{LoS} depends on the light radiance angle ϕ, and is inversely proportional to the distance D between the transmitter and receiver. When $\phi = 0$, the LoS component η_{LoS} achieves the maximum channel power at the same distance.

The SCO makes the inaccurate channel estimation in the frame detection. Thus, we need to improve channel estimation successively. In the next section, SCO and channels are considered to be jointly estimated.

C. Sampling Clock Synchronization

The training sequences that are used for frame detection can be employed again in this section to perform joint ML SCO and channel estimation. With correct timing index, the joint SCO and channel estimations are performed by minimizing the cost function as follows:

$$J(\tau, \mathbf{h}) = ||\mathbf{y} - \mathbf{G}(\tau)\mathbf{X}\mathbf{h}||_F^2. \tag{24}$$

As the SCO is between -0.5 and 0.5, we use the trial value of $\tilde{\tau}$ and the training sequences $\mathbf{X}_P$ to estimate the channel with $\tilde{\tau}$ as follows:

$$\mathbf{h}(\tilde{\tau}) = \left(\mathbf{X}_P^T\mathbf{G}^T(\tilde{\tau})\mathbf{G}(\tilde{\tau})\mathbf{X}_P\right)^{-1}\mathbf{X}_P^T\mathbf{G}^T(\tilde{\tau})\mathbf{y}. \tag{25}$$

By substituting Eqs. (25) into (24), the estimate of SCO $\hat{\tau}$ is to minimize the cost function as follows:

$$\hat{\tau} = \underset{\tilde{\tau}\in(-0.5,\,0.5)}{\arg\min}\ ||\mathbf{y} - \mathbf{G}(\tilde{\tau})\mathbf{X}_P\mathbf{h}(\tilde{\tau})||_F^2. \tag{26}$$

By substituting Eqs. (26) into (25), the channel estimation is performed as follows:

$$\hat{\mathbf{h}} = \left(\mathbf{X}_P^T\mathbf{G}^T(\hat{\tau})\mathbf{G}(\hat{\tau})\mathbf{X}_P\right)^{-1}\mathbf{X}_P^T\mathbf{G}^T(\hat{\tau})\mathbf{y}. \tag{27}$$

In a multiple input multiple output (MIMO) system, where there are multiple transmitters and receivers, Eq. (13) is still applicable. However, using Eq. (13) leads to extremely high computational complexity in the MIMO case. The proposed timing synchronization approach can divide the multi-dimensional problem into a number of one-dimensional problems, greatly reducing the complexity for MIMO systems. Therefore, the proposed approach can easily be extended to MIMO systems.

D. Cramér-Rao Lower Bound

As the SCO estimation and the channel estimation in Eqs. (26) and (27) are unbiased, CRBs [26] can be employed to provide a performance benchmark as lower bound. We derive the CRBs in terms of closed-form expression for the joint estimation of SCO τ and channel $\mathbf{h}$. As the variance of any unbiased estimator is as high as the inverse of the Fisher Information matrix, the CRB lower bound corresponds to the inverse of Fisher Information matrix. As τ and $\mathbf{h}$ are real, the estimation vector $\boldsymbol{\theta}$ can be expressed as

$$\boldsymbol{\theta} = [\tau, \mathbf{h}]^T. \tag{28}$$

Using the received signals, the corresponding Fisher Information matrix for the estimate of vector can be written as follows: [26]

$$\mathbf{F}_{\mathbf{IM}} = \frac{2}{\sigma^2}\left[\frac{\partial\mathbf{y}^T}{\partial\boldsymbol{\theta}}\frac{\partial\mathbf{y}}{\partial\boldsymbol{\theta}^T}\right]. \tag{29}$$

In the Fisher Information matrix, we should note that, 1), the diagonal elements are non-negative; and 2), the diagonal elements of the inverse of Fisher Information matrix are the bounds for the joint estimates of τ and $\mathbf{h}$. The (u, v) component of Fisher Information matrix is expressed as

$$[\mathbf{F}_{\mathbf{IM}}]_{u,v} = \frac{2}{\sigma^2}\left[\frac{\partial\mathbf{y}^T}{\partial[\boldsymbol{\theta}]_u}\frac{\partial\mathbf{y}}{\partial[\boldsymbol{\theta}]_v{}^T}\right]. \tag{30}$$

Define $\mathbf{A} = \frac{\partial\mathbf{G}(\tau)}{\partial\tau}\mathbf{X}_P$ and $\mathbf{B} = \mathbf{G}(\tau)\mathbf{X}_P$. Here, we have $\frac{\partial^2\mathbf{y}}{\partial\tau^2} = \mathbf{h}^H\mathbf{A}^H\mathbf{A}\mathbf{h}$, $\frac{\partial^2\mathbf{y}}{\partial\tau\,\partial\mathbf{h}} = \mathbf{h}^H\mathbf{A}^H\mathbf{B}$, $\frac{\partial^2\mathbf{y}}{\partial\mathbf{h}\,\partial\tau} = \mathbf{B}^H\mathbf{A}\mathbf{h}$, and $\frac{\partial^2\mathbf{y}}{\partial\mathbf{h}^2} = \mathbf{B}^H\mathbf{B}$.

The Fisher Information matrix yields:

$$\mathbf{F}_{\mathbf{IM}} = \frac{2}{\sigma^2}\begin{bmatrix}\mathbf{h}^T\mathbf{A}^T\mathbf{A}\mathbf{h} & \mathbf{h}^T\mathbf{A}^T\mathbf{B}\\ \mathbf{B}^T\mathbf{A}\mathbf{h} & \mathbf{B}^T\mathbf{B}\end{bmatrix}. \tag{31}$$

Define $\alpha = (\mathbf{h}^T\mathbf{A}^T\mathbf{\Delta_B}\mathbf{A}\mathbf{h})^{-1}$ with $\mathbf{\Delta_B} = \mathbf{I} - \mathbf{B}(\mathbf{B}^T\mathbf{B})^{-1}\mathbf{B}^T$, $\boldsymbol{\beta} = (\mathbf{B}^T\mathbf{B})^{-1}\mathbf{B}^T\mathbf{A}\mathbf{h}$, and $\mathbf{C}_h = \mathbf{B}^T\mathbf{B}$. The CRB of the joint estimation of τ and $\mathbf{h}$ is the inverse of the Fisher Information matrix, as shown in Appendix B, and this leads to:

$$\mathbf{C_{RB}} = \frac{\sigma^2}{2}\begin{bmatrix} \alpha & \alpha\boldsymbol{\beta}^T \\ \alpha\boldsymbol{\beta} & \mathbf{C}_h^{-1} + \alpha\boldsymbol{\beta}\boldsymbol{\beta}^T \end{bmatrix}. \tag{32}$$

As the diagonal elements of the $\mathbf{C_{RB}}$ matrix are corresponding to the bounds for the estimations of τ and $\mathbf{h}$, the CRB of the SCO estimation $\mathrm{C_{RB}}(\tau)$ is the $(1,1)$ entry of $\mathbf{C_{RB}}$ in Eq. (32), given as follows:

$$\begin{aligned}\mathrm{C_{RB}}(\tau) &= \frac{\sigma^2}{2}\alpha \\ &= \frac{\sigma^2}{2}\left(\mathbf{h}^T\mathbf{A}^T\mathbf{\Delta_B}\mathbf{A}\mathbf{h}\right)^{-1}.\end{aligned} \tag{33}$$

The CRB of the channel estimation $\mathbf{C_{RB}}(\mathbf{h})$ is the $(2,2)$ entry of $\mathbf{C_{RB}}$ in Eq. (32), given as follows:

$$\mathbf{C_{RB}}(\mathbf{h}) = \frac{\sigma^2}{2}\left(\mathbf{C}_h^{-1} + \alpha\boldsymbol{\beta}\boldsymbol{\beta}^H\right). \tag{34}$$

It can be observed from Eqs. (33) and (34) that the high channel gains and the strong power of training sequences can minimize the CRB of joint SCO and channel estimations.

E. Training Sequence Design

The objective of training sequence design is to minimize the CRBs with respect to the SCO and channel estimations. It is observed in Eq. (32) that $\mathbf{C_{RB}}(\mathbf{h})$ is affected by $\mathrm{C_{RB}}(\tau)$. Minimizing $\mathrm{C_{RB}}(\tau)$ corresponds to minimizing $\mathbf{C_{RB}}(\mathbf{h})$. Thus, we design a set of training sequences $\hat{\mathbf{X}}_P$ to minimize $\mathrm{C_{RB}}(\tau)$ as follows:

$$\hat{\mathbf{X}}_P = \frac{\sigma^2}{2}\arg\min_{\mathbf{X}_P}\left\{\left(\mathbf{h}^T\mathbf{A}^T\mathbf{\Delta_B}\mathbf{A}\mathbf{h}\right)^{-1}\right\}. \tag{35}$$

In other words, the optimum set of training sequences can be found by maximizing the eigenvalue of $\mathbf{h}^T\mathbf{A}^T\mathbf{\Delta_B}\mathbf{A}\mathbf{h}$. As the channel $\mathbf{h}$ is unknown, it is not possible to find a set of optimal training sequences that optimize Problem (35) with general $\mathbf{h}$. In order to make Problem (35) tractable, we can simplify Problem (35) to

$$\hat{\mathbf{X}}_P = \frac{\sigma^2}{2||\mathbf{h}||_F^2}\arg\max_{\mathbf{X}_P}\left\{\mathrm{trace}\left\{\mathbf{A}^T\mathbf{\Delta_B}\mathbf{A}\right\}\right\}. \tag{36}$$

Using Eqs. (7) and (11), $\mathbf{X}_P$ can be expressed by the frequency-domain signal $\mathbf{s}$. The optimization problem can be formulated to the design of the frequency-domain training sequences $\mathbf{s}$. Let $\mathbf{R}(\tau) = \frac{\partial\mathbf{G}(\tau)}{\partial\tau}$. Using Eq. (7) and making some arrangements, considering the effect of $\mathbf{A}^T\mathbf{A}$ in Problem (36), we can formulate the following problem to optimize training sequences as

$$\begin{aligned}\hat{\mathbf{s}} = \arg\max_{\mathbf{s}}\ &\left\{\mathrm{trace}\left\{\mathbf{F}_L^H\mathrm{diag}\{\mathbf{s}^H\}\mathbf{F}\mathbf{R}^T(\tau)\mathbf{R}(\tau)\mathbf{F}^H\mathrm{diag}\{\mathbf{s}\}\mathbf{F}_L\right\}\right\}, \\ &\text{subject to } \mathbf{s}^H\mathbf{s} = 1.\end{aligned} \tag{37}$$

We only consider the dominate and significant component $\mathbf{R}^T(\tau)\mathbf{R}(\tau)$ in (37) for the optimization of training sequences $\mathbf{s}$. We can find the solution to (37) as the eigenvector of $\mathbf{R}^T(\tau)\mathbf{R}(\tau)$ with respect to the maximum eigenvalue [27]. Define $\lambda_{\max}\{\mathbf{R}^T(\tau)\mathbf{R}(\tau)\}$ and $\mathbf{v}_{\max}\{\mathbf{R}^T(\tau)\mathbf{R}(\tau)\}$ as the largest eigenvalue and the associated eigenvector of $\mathbf{R}^T(\tau)\mathbf{R}(\tau)$, respectively. Then, we can find an optimization for Problem (37) as follows:

$$\hat{\mathbf{s}} = \mathbf{F}\mathbf{v}_{\max}\{\mathbf{R}^T(\tau)\mathbf{R}(\tau)\}. \tag{38}$$

Although the solution is not an optimal solution to the original hard coupling Problem (35). However, we provide a tractable way to establish a solution which is still meaningful in engineering applications. Note that the training sequence design depends on $\mathbf{R}^T(\tau)\mathbf{R}(\tau)$ with respect to τ which is not known in advance. However, $\mathbf{R}^T(\tau)\mathbf{R}(\tau)$ is independent of τ, with a large number of N and Q [28]. The variations of τ have no significant impact on the performance [28]. Thus, we use the range $0 - 0.1$ which sits at the center of the SCO between -0.5 and 0.5 to design the training sequences.

V. Performance Analysis

A. Complexity Analysis

For frame detection, MNCP results in (N^2P) multiplication operations, while MRSP leads to $(N^2\ P^2)$ multiplication operations. As can be seen, MNCP exhibits a P-fold complexity reduction, compared to MRSP. This is because Eq. (16) is not required in MNCP. When $P = 1$, MRSP becomes SMRSP, achieving (N^2) multiplication operations. The proposed sampling clock synchronization method requires $(N^4\ Q^3\frac{1}{\Delta})$ operations.

With each search, the proposed optimum timing synchronization in Eq. (13) needs $(N^6\ Q^3\ P^2\frac{1}{\Delta})$ operations, with Δ denoting the step size of the search for the SCO. Compared to the optimum method, the proposed sub-optimal approach can achieve a reduction of at least approximately $(N^2\ P^2)$ multiplication operations. This is equal to about $589,824$ multiplication operations reduction when $N = 64$ and $P = 12$. These parameters are used in the simulation setup in Section VI.

B. Performance Analysis for Frame Detection

1) Discussion of Training Length P: The proposed MRSP and MNCP frame detection methods can only work if the training matrix $\mathbf{X}_P$ of size $N \times P$ is singular.

- When $P = N$, $\mathbf{X}_P$ is square. Eqs. (15) and (16) are independent of $\tilde{\theta}_\epsilon$. MRSP and MNCP cannot work.
- When $P \mapsto N$, the proposed MRSP and MNCP provide worse performance, verified in Fig. 4.
- When $P \mapsto 1$, MNCP cannot perform, as sufficient training length P is required to generate the number of channel paths L, *i.e.*, $P \geq L$, as shown in Fig. 4.
- When $P = 1$, MRSP becomes SMRSP.

2) Impact of DC Bias Ratio K: When DC bias ratio K is low, all frame detection methods provide poor performance, as less optical power is used, as shown in Eq. (40). When a high level of the DC bias ratio is used, the DC power of training signals increases. The component of $(\mathbf{X}_P^T\mathbf{X}_P)^{-1}$ includes a number of stronger negative coefficients, which

TABLE I
ESTIMATORS WITH ANALYTICAL PARAMETERS (SYN.: SYNCHRONIZATION, EST.: ESTIMATION, CS: CHANNEL ESTIMATION)

Item	Frame Detection			Sampling Clock Syn.	
	MRSP	SMRSP	MNCP	SCO est.	CS
DC bias ratio K	1	2	1	5	1
Training sequence length P	1-12	1	12	6	6

is multiplied to the noise in Eq. (15) for the MNCP and MRSP techniques. The high-valued negative coefficients do not reduce the noise power. The MNCP and MRSP techniques cannot perform well. Thus, there is a careful selection of DC bias ratio, as a too low or too high level of DC bias ratio K makes the performance of the MRSP and MNCP techniques become worse. For SMRSP, the noise is reduced by the scalar of $\mathbf{x}^T\mathbf{x} \approx K^2\mathrm{E}\{\tilde{x}^2(n)\}$ as shown in Eq. (17), which is proportional to the DC bias ratio K. Thus, SMRSP provides performance improved with higher value of K used. The impact of K on a number of frame detection methods is verified in Fig. 3.

3) Discussion of Noise Reduction: The MNCP technique reduces the noise by $\left(\mathbf{X}_P^T\mathbf{X}_P\right)^{-1}\mathbf{X}_P^T$, while the MRSP technique does not reduce the noise power, as the component of $\mathbf{X}_P\left(\mathbf{X}_P^T\mathbf{X}_P\right)^{-1}\mathbf{X}_P^T$ is multiplied to the noise. For this reason, the MNCP technique provides better performance than the MRSP technique. The SMRSP frame detection reduces the noise by a scalar of $\mathbf{x}^T\mathbf{x}$. However, some negative coefficients have strong power in $(\mathbf{X}_P^T\mathbf{X}_P)^{-1}\mathbf{X}_P^T$ for the MNCP technique, which does not reduce the noise power. Thus, the SMRSP frame detection provides better performance than MNCP and MRSP techniques, verified in Fig. 2.

C. Performance Analysis for Sampling Clock Synchronization

1) Discussion of Training Length P: Let $\mathbf{B} = \mathbf{U}\mathbf{\Lambda}\mathbf{V}^T$ be the singular value decomposition (SVD), where $\mathbf{\Lambda}$ denotes the diagonal singular matrix of size $QN \times P$, $\mathbf{U}$ and $\mathbf{V}$ denote unitary matrices of sizes $QN \times QN$ and $P \times P$, respectively. Let $\tilde{\mathbf{U}} = \mathbf{U}(1 : QN, 1 : P)$. After some mathematical simplification as shown in Appendix C, Eq. (36) can be rewritten as follows:

$$\hat{\mathbf{X}}_P = \frac{\sigma^2}{2||\mathbf{h}||_F^2}\arg\max_{\mathbf{X}_P}\left\{\mathrm{trace}\left\{\mathbf{A}^T\left(\mathbf{I} - \tilde{\mathbf{U}}\tilde{\mathbf{U}}^T\right)\mathbf{A}\right\}\right\}. \quad (39)$$

$\tilde{\mathbf{U}}$ is the $QN \times P$ sub-matrix of an unitary matrix. When $P \mapsto N$, $\tilde{\mathbf{U}}\tilde{\mathbf{U}}^T$ tends towards an identity matrix, *i.e.*, $(\mathbf{I} - \tilde{\mathbf{U}}\tilde{\mathbf{U}}^T) \mapsto \mathbf{0}$. Problem (39) cannot be optimized. When $P \mapsto 1$, using Eqs. (26) and (27) does not generate a sufficient number of channel paths. Therefore, the training sequence length P should be larger than L, and much less than N. The impact of training sequence length P is verified in Fig. 7.

2) Impact of DC Bias Ratio K: Since $\mathrm{C_{RB}}(\tau)$ is a scalar, a high DC bias ratio enhances the power of training signals, and minimizes the $\mathrm{C_{RB}}(\tau)$ of the SCO estimation.

For channel estimation, the $\mathbf{C_{RB}(h)}$ includes $\mathbf{C}_h^{-1}$ and $\alpha\boldsymbol{\beta}\boldsymbol{\beta}^H$, as shown in Eq. (34). With a large size of $\mathbf{G}(\tau)$, it holds that $\mathbf{G}^T(\tau)\mathbf{G}(\tau) \approx \mathbf{I}$. Thus, we have $\mathbf{C}_h^{-1} \approx (\mathbf{X}_P^T\mathbf{X}_P)^{-1}$. Minimizing α, *i.e.*, $\mathrm{C_{RB}}(\tau)$, results in $||\alpha\boldsymbol{\beta}\boldsymbol{\beta}^H||_F^2 \ll ||(\mathbf{X}_P^T\mathbf{X}_P)^{-1}||_F^2$. Thus, the CRB of the channel estimation depends on the component of $\mathbf{C}_h^{-1}$ or $(\mathbf{X}_P^T\mathbf{X}_P)^{-1}$ rather than $\alpha\boldsymbol{\beta}\boldsymbol{\beta}^H$. If a low level of DC bias ratio K is used in training sequences, less optical power is used, as shown in Eq. (40). The proposed channel estimation provides poor performance. However, a high level of DC bias ratio does not minimize the CRB of the channel estimation. This is because the high DC bias makes the high power of negative coefficients in $(\mathbf{X}_P^T\mathbf{X}_P)^{-1}$, resulting in the increased value of $\mathbf{C_{RB}(h)}$. Thus, the DC bias ratio K should be carefully selected to trade off the SCO estimation and the channel estimation. The impact of DC bias ratio K is verified in Fig. 8.

VI. SIMULATION RESULTS

We use Monte-Carlo simulations to analyze the performance of the proposed timing synchronization methods for DCO-OFDM systems. Unless otherwise stated, the simulations assume that a data frame contains 256 DCO-OFDM blocks of $N = 64$ subcarriers. The CP length is $L_{\mathrm{CP}} = 16$. An oversampling ratio of $Q = 4$ is used. A single DCO-OFDM block is used as training, resulting in a training overhead of $1/256 = 0.39\%$. The DC bias ratio is set as $K = 1$. The training sequence length is $P = 12$ or $P = 6$. However, the optimum selection of K and P depends on method used. Table I shows the optimal selection of K and P for a number of frame detection and sampling clock synchronization methods. A raised cosine filter is employed, with roll off factor of 0.2. The symbol rates are 500 Msymbols/s. A step size of $\Delta = 0.001$ is used to search for the SCO. The training sequences are generated using SCO $\tau = 0$ or $\tau = 0.1$.

The mean squared error (MSE) between the true and estimated SCOs, is defined as $\mathrm{MSE} = \mathrm{E}\{(\tau - \hat{\tau})^2\}$. The MSE of channel estimation is defined as $\mathrm{MSE} = \mathrm{E}\{(\mathbf{h} - \hat{\mathbf{h}})^T(\mathbf{h} - \hat{\mathbf{h}})\}$. Energy per bit for optical power is denoted by $E_{b,\mathrm{opt}}$, while electrical power by $E_{b,\mathrm{ele}}$. The optical power is obtained from the electrical power as follows [8]:

$$\frac{E_{b,\mathrm{opt}}}{N_0} = \frac{K^2}{1+K^2}\frac{E_{b,\mathrm{ele}}}{N_0}. \quad (40)$$

The 3-dB cutoff bandwidth of LED is $f_b = 81.5$ MHz [19]. The room size is 5 m × 5 m × 3 m (length × width × height) [23]. The LED is located on the ceiling, with the coordinate (3 m, 3 m, 3 m). The receiver is on the desk of height 1 m facing upwards. A transmitter's light radiance angle of $\phi = 40$ degrees is used, while the receiver's corresponding light incidence angle is $\varphi = 60$ degrees [22]–[24]. The receiver detection area is $A_{\mathrm{rx}} = 1$ cm^2 is used. The half-power semi-angle of LED is $\phi_{1/2} = 60$ degrees. The average reflectivity of walls is assumed to be $\rho = 0.8$. An optical filter gain of

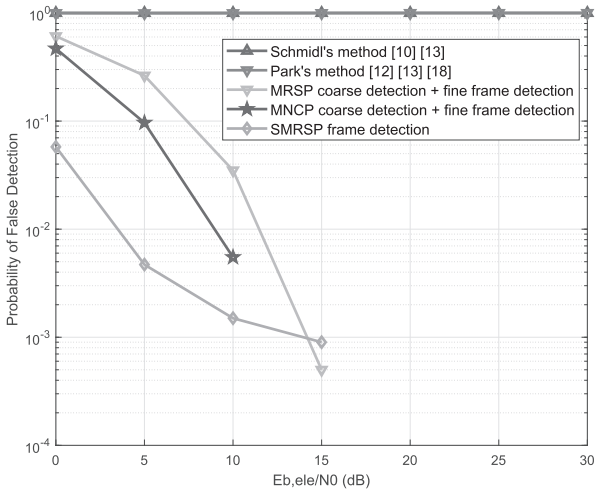

Fig. 2. Probability of false frame detection performance of the proposed MRSP, SMRSP and MNCP based frame detection methods, with $P = 12$ training sequence length and $K = 1$ DC bias ratio, in the presence of SCO.

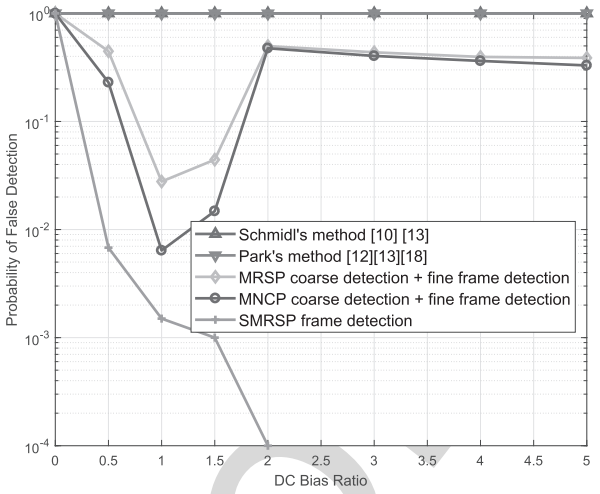

Fig. 3. Impact of DC bias ratio K on the probability of false frame detection performance of the proposed MRSP, SMRSP and MNCP based frame detection methods, with $P = 12$ training sequence length and $E_{b,\text{ele}}/N_0 = 10$ dB, in the presence of SCO.

$T(\phi) = 1$ is considered at the transmitter, while a concentrator gain of $G(\varphi) = 1$ is used at the receiver.

A. Performance of Frame Detection

In Fig. 2, the probability of false frame detection of the proposed MRSP, SMRSP and MNCP frame detection schemes is demonstrated, in comparison with Schmidl's method and Park's method [10], [12], [13], [18], in the presence of SCO. The MRSP and MNCP frame detection schemes result in performance significantly better than Schmidl's method and Park's method. MNCP outperforms MRSP in terms of 3 dB gains. This is because MNCP can reduce noise power, as discussed in Subsection V-B-3). SMRSP is robust against the effect of SCO when no fine frame detection is in place. It provides a better performance than MRSP and MNCP at low $E_{b,\text{ele}}/N_0$. This is because SMRSP can suppress noise power, more than MNCP, as discussed in Subsection V-B-3). Schmidl's and Park's methods are not robust against the combined effect of SCO and the low-pass characteristic of LED.

Fig. 3 demonstrates the impact of DC bias ratio on the false frame detection probability performance when using MRSP, SMRSP and MNCP, in the presence of SCO, with $E_{b,\text{ele}}/N_0 =$ 10 dB and $P = 12$. MRSP and MNCP frame detection approaches demonstrate a concave with the variations of DC bias ratio, and achieve the best performance at $K = 1$ DC bias ratio. There is significant improvement using SMRSP when a higher DC bias ratio used. This is because the noise is reduced by the scalar of $\mathbf{x}^T\mathbf{x} \approx K^2\text{E}\{\tilde{x}^2(n)\}$, which is proportional to the DC bias ratio K, as discussed in Subsection V-B-2).

In Fig. 4, the impact of training sequence length P on the performance of false frame detection probability for the proposed methods is demonstrated, in the presence of SCO, with $E_{b,\text{ele}}/N_0 = 10$ dB and $K = 1$. SMRSP is shown with $P = 1$ training sequence length, as a special case of MRSP. With short training sequence length, MRSP provides better performance than MNCP. This is because MNCP requires

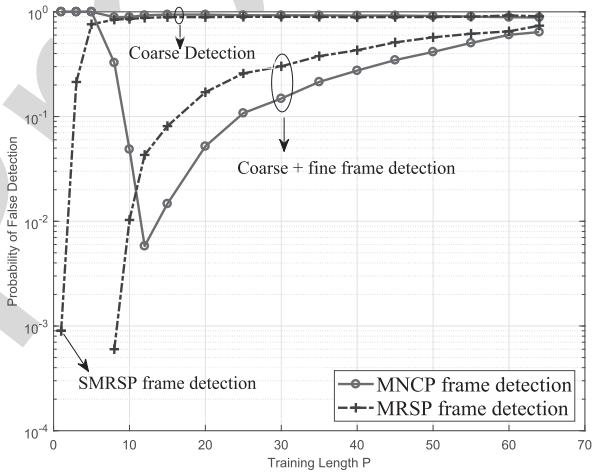

Fig. 4. Impact of training sequence length P on the probability of false frame detection performance of the proposed MRSP, SMRSP, MNCP based frame detection methods, with $K = 1$ DC bias ratio and $E_{b,\text{ele}}/N_0 = 10$ dB, in the presence of SCO.

sufficient training length to generate the total number of channel paths for frame detection. SMRSP can minimize part of difference between the received and reconstructed signals to perform frame detection. When P becomes large and close to N, the proposed methods provide worse performance, because the training matrix is close to square. This is consistent with the discussion in Subsection V-B-1).

B. Performances of Sampling Clock synchronization

Figs. 5 and 6 demonstrate the MSE performance of the proposed SCO estimation and channel estimation methods, respectively, with $K = 1$ DC bias ratio and $P = 6$ training sequence length. From $E_{b,\text{ele}}/N_0 s = 0$ dB to 15 dB, there is a big performance gap. This is due to the false frame detection, affecting the MSE performance of the proposed SCO estimation and channel estimation methods. From $E_{b,\text{ele}}/N_0 s = 15$ dB to 30 dB, the proposed SCO

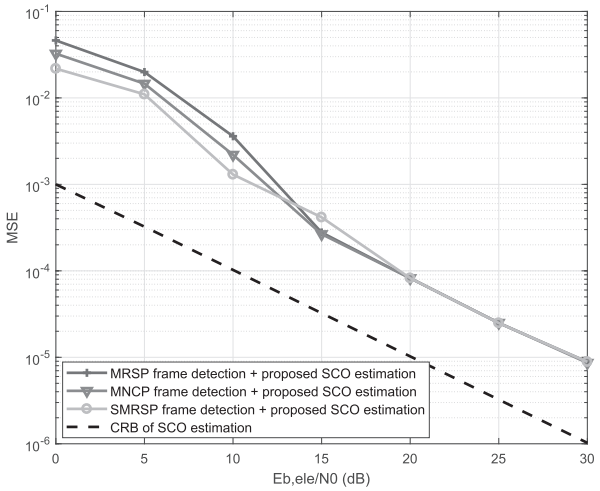

Fig. 5. MSE performance of the proposed SCO estimation, in comparison to the CRB of SCO estimation, with $K = 1$ DC bias ratio and $P = 6$ training sequence length.

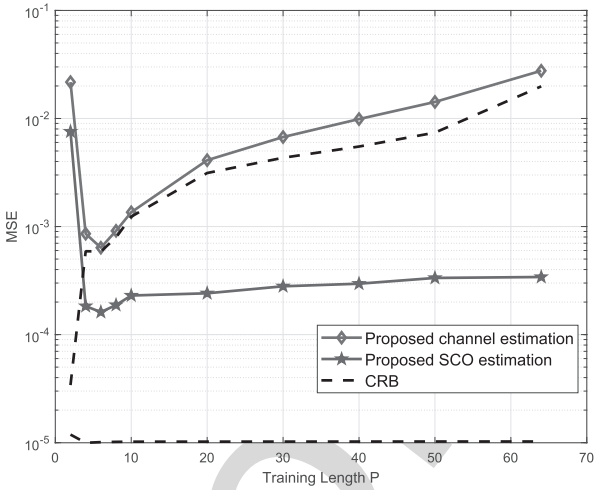

Fig. 7. Impact of the training sequence length P on the MSE performance of the proposed SCO and channel estimation methods, with $K = 1$ DC bias ratio and $E_{b,\text{ele}}/N_0 = 20$ dB.

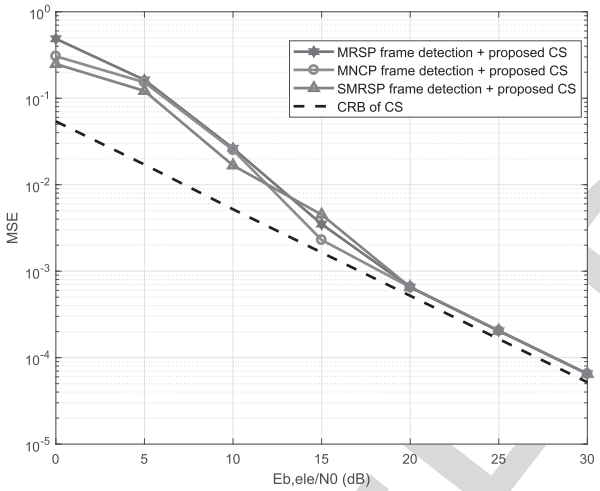

Fig. 6. MSE performance of the proposed channel estimation, in comparison to the CRB for channel estimation, with $K = 1$ DC bias ratio and $P = 6$ training sequence length. CS refers to channel estimation in the legend.

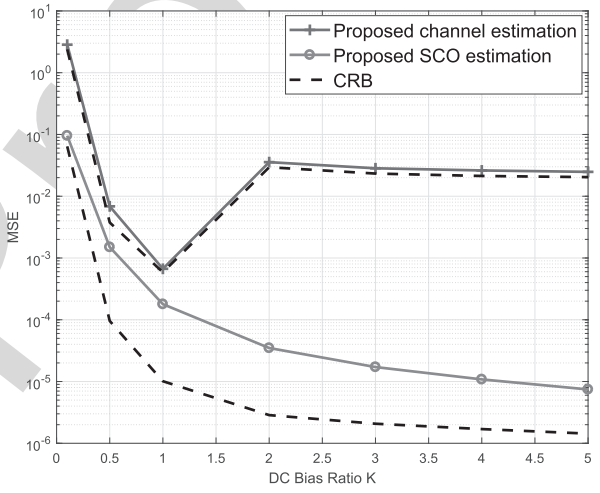

Fig. 8. Impact of the DC bias ratio K on the MSE performance of the proposed SCO and channel estimation methods, with $P = 6$ training sequence length and $E_{b,\text{ele}}/N_0 = 20$ dB.

estimation and channel estimation schemes alongside the proposed frame detection can provide MSE performance, close to their CRBs.

Fig. 7 demonstrates the impact of training sequence length P on the MSE performance of the proposed SCO and channel estimation schemes, with $E_{b,\text{ele}}/N_0 = 20$ dB and $K = 1$ DC bias ratio. The proposed SCO and channel estimation schemes show the best performance at training sequence length $P = 6$. This is because the sufficient training length P is required to generate the total number of channel paths. When P is too large, we have $(\mathbf{I} - \tilde{\mathbf{U}}\tilde{\mathbf{U}}^T) \approx \mathbf{0}$ in Eq. (39). Problem (39) cannot be optimized. The proposed SCO and channel estimation schemes cannot work. This is consistent with the discussion in Subsection V-C-1).

Fig. 8 showcases the impact of DC bias ratio K on the MSE performance of the proposed SCO and channel estimation schemes, with $E_{b,\text{ele}}/N_0 = 20$ dB and $P = 6$. The proposed SCO estimation scheme provides performance improvements when the DC bias ratio increases. This is due to two reasons: One reason is that greater optical power is used with a higher level of DC bias ratio. The other reason is that at the same time with the addition of a larger DC bias, the DC signal power can be enhanced, minimizing the $\mathrm{C}_{\mathrm{RB}}(\tau)$ of the SCO estimation. Thus, the proposed SCO estimation method improves. This is consistent with the discussion in Subsection V-C-2). Also, it is shown that the proposed SCO estimation scheme yield performance that is close to the CRB. For the proposed channel estimation method, a high level of DC bias ratio does not improve the performance. This is because the high DC bias makes the high power of negative coefficients in $(\mathbf{X}_P^T\mathbf{X}_P)^{-1}$, resulting in the increased value of $\mathbf{C_{RB}}(\mathbf{h})$, as discussed in Subsection V-C-2). Thus, the performance of the proposed channel estimation is shown to be concave. The best performance can be achieved at $K = 1$.

C. BER Performance of Proposed Timing Synchronization

In Fig. 9, the BER performance of the proposed timing synchronization process is demonstrated with

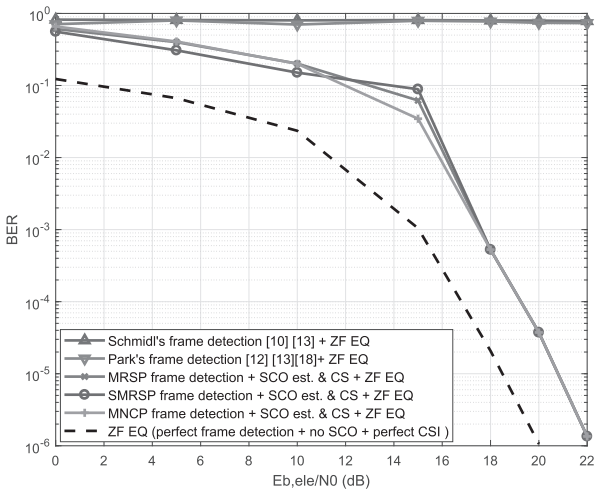

Fig. 9. BER performance of the proposed timing synchronizing scheme. EQ refers to equalization; CE refers to channel estimation and est. refers to estimation.

16 QAM modulation. The zero forcing (ZF) based equalization method with perfect frame detection, no SCO and perfect CSI is used as benchmark. The proposed timing synchronization process includes three frame detection methods, *i.e.*, MRSP, SMRSP and NMCP, and the proposed SCO and channel estimation methods. With a training overhead of 0.39%, a number of proposed timing synchronization schemes provide BER performance significantly better than Schmidl's and Park's methods [10], [12], [13], [18], and performance close to the ZF equalization based case with perfect CSI, no SCO and perfect frame detection.

VII. Conclusion

In this paper, we have proposed a timing synchronization mechanism for DCO-OFDM LiFi systems. By using a single training DCO-OFDM block, frame detection and SCO estimation can be performed together jointly with channel estimation. The proposed timing synchronization techniques provide BER performance close to the ideal case with perfect CSI, no SCO and perfect frame detection. The proposed new frame detection methods significantly outperform Schmidl's method and Park's method in terms of probability of false frame detection, and demonstrate the robustness against the SCO and the low-pass characteristic of the optical front-ends. The proposed SCO estimation and channel estimation methods result in performance close to CRBs. The proposed timing synchronization mechanism allows harnessing of trade-offs between estimation accuracy, spectral efficiency, energy efficiency, and complexity. In future work, we consider extending the timing synchronization to MIMO systems.

Appendix A
Proof of Theorem 1

Let $x(n,l)$ denote the transmitted symbol on the n-th row and l-th column of $\mathbf{X}$. Let $\mathbf{X} = [\mathbf{x}(0), \mathbf{x}(1), \ldots, \mathbf{x}(N-1)]^T$, with $\mathbf{x}(n) = [x(n,0), x(n,1), \ldots, x(n,L-1)]$. The transmitted signal vector can be written as $\mathbf{x} = [x(0,0), x(1,0), \ldots, x(N-1,0)]^T$. Eq. (17) can be re-written as follows:

$$h(\tilde{\theta}_\epsilon) = \left(\mathbf{x}^T\mathbf{x}\right)^{-1} \times \{r(0)h(0) + r(1)h(1) + \ldots r(L-1)h(L-1)\} \quad (41)$$

where $r(0) = x^2(0,0) + x^2(1,0) + \ldots + x^2(N-1,0)$, $r(1) = x(0,0)x(0,1) + \ldots x(N-1,0)x(N-1,1)$, ..., $r(L-1) = x(0,0)x(0,L-1) + \ldots x(N-1,0)x(N-1,L-1)$. Since $\mathbf{x}^T\mathbf{x} = r(0)$, the reconstructed signal in Eq. (18) is given as follows:

$$h(\tilde{\theta}_\epsilon)\mathbf{x} = h(0)\mathbf{x} + \left(\mathbf{x}^T\mathbf{x}\right)^{-1} \times \{r(1)h(1) + \ldots r(L-1)h(L-1)\}\mathbf{x}. \quad (42)$$

The first term of Eq. (42) is the part of received signals $\mathbf{y}_N(\tilde{\theta}_\epsilon)$, while the second term is the difference. The SMRSP based frame detection is to cancel the first term, by treating the second term as noise. If $f_{b_1} < f_{b_2}$, from Eq. (5), we can obtain

$$\frac{h_{\mathrm{LED}}(t, f_{b_2})}{h_{\mathrm{LED}}(t, f_{b_1})} = e^{j2\pi t(f_{b_1} - f_{b_2})} < 1. \quad (43)$$

We can see $h_{\mathrm{LED}}(t, f_{b_2}) < h_{\mathrm{LED}}(t, f_{b_1})$ with a fixed t and $t \neq 0$. Thus, the higher cutoff bandwidth leads to lower channel response of $h(1), \ldots, h(L-1)$. The power of the second term of Eq. (42) is reduced. The difference between the received and reconstructed signals is minimized. The SMRSP frame detection improves. When the cutoff bandwidth is as high as possible, we have $e^{-j2\pi f_b t} \approx 0$ with a fixed t and $t \neq 0$, resulting in $h(1), \ldots, h(L-1) \mapsto 0$. MRSP becomes SMRSP. This proves Theorem 1.

Appendix B
Mathematical Derivations of $\mathbf{C_{RB}}$

The Fisher Information matrix in Eq. (31) can be rewritten as follows:

$$\mathbf{F_{IM}} = \frac{2}{\sigma^2}\begin{bmatrix} C_\tau & \boldsymbol{\Upsilon}^T \\ \boldsymbol{\Upsilon} & \mathbf{C}_h \end{bmatrix} \quad (44)$$

where $C_\tau = \mathbf{h}^H\mathbf{A}^H\mathbf{A}\mathbf{h}$, $\mathbf{C}_h = \mathbf{B}^H\mathbf{B}$ and $\boldsymbol{\Upsilon} = \mathbf{B}^H\mathbf{A}\mathbf{h}$. According to the matrix inverse lemma [29], we can obtain the inverse of Fisher Information matrix:

$$\begin{aligned}\frac{2}{\sigma^2}\mathbf{F}_{\mathbf{IM}}^{-1} &= \begin{bmatrix}\mathbf{0}_{1\times L} \\ \mathbf{I}_{L\times L}\end{bmatrix}\mathbf{C}_h^{-1}\left[\mathbf{0}_{L\times 1}, \mathbf{I}_{L\times L}\right] \\ &\quad + \begin{bmatrix} 1 \\ -\mathbf{C}_h^{-1}\boldsymbol{\Upsilon}\end{bmatrix}\left(C_\tau - \boldsymbol{\Upsilon}^T\mathbf{C}_h^{-1}\boldsymbol{\Upsilon}\right)^{-1}\left[1 - \boldsymbol{\Upsilon}^T\mathbf{C}_h^{-1}\right] \\ &= \begin{bmatrix} 0 & \mathbf{0}_{1\times L} \\ \mathbf{0}_{L\times 1} & \mathbf{C}_h^{-1}\end{bmatrix} + \left(C_\tau - \boldsymbol{\Upsilon}^T\mathbf{C}_h^{-1}\boldsymbol{\Upsilon}\right)^{-1} \\ &\quad \times \begin{bmatrix} 1 & -\boldsymbol{\Upsilon}^T\mathbf{C}_h^{-1} \\ -\mathbf{C}_h^{-1}\boldsymbol{\Upsilon} & \mathbf{C}_h^{-1}\boldsymbol{\Upsilon}\boldsymbol{\Upsilon}^T\mathbf{C}_h^{-1}\end{bmatrix} \quad (45)\end{aligned}$$

Let $\alpha \triangleq \left(C_\tau - \boldsymbol{\Upsilon}^T\mathbf{C}_h^{-1}\boldsymbol{\Upsilon}\right)^{-1} = \left(\mathbf{h}^H\mathbf{A}^H\boldsymbol{\Delta}_{\mathbf{B}}\mathbf{A}\mathbf{h}\right)^{-1}$ with $\boldsymbol{\Delta}_{\mathbf{B}} = \mathbf{I} - \mathbf{B}(\mathbf{B}^T\mathbf{B})^{-1}\mathbf{B}^T$ and $\boldsymbol{\beta} \triangleq -\mathbf{C}_h^{-1}\boldsymbol{\Upsilon} = (\mathbf{B}^H\mathbf{B})^{-1}\mathbf{B}^H\mathbf{A}\mathbf{h}$. Eq. (45) can be rewritten:

$$\frac{2}{\sigma^2}\mathbf{F}_{\mathbf{IM}}^{-1} = \begin{bmatrix} 0 & \mathbf{0}_{1\times K} \\ \mathbf{0}_{K\times 1} & \mathbf{C}_h^{-1}\end{bmatrix} + \alpha\begin{bmatrix} 1 & \boldsymbol{\beta}^H \\ \boldsymbol{\beta} & \boldsymbol{\beta}\boldsymbol{\beta}^H\end{bmatrix}. \quad (46)$$

Thus, the joint CRB of the SCO estimation and channel estimation is expressed:

$$\mathbf{C_{RB}} = \frac{\sigma^2}{2}\begin{bmatrix} \alpha & \alpha\boldsymbol{\beta}^H \\ \alpha\boldsymbol{\beta} & \mathbf{C}_h^{-1} + \alpha\boldsymbol{\beta}\boldsymbol{\beta}^H \end{bmatrix}. \tag{47}$$

This proves Eq. (32).

Appendix C
Proof of Eq. (39)

It holds that

$$\begin{aligned}(\mathbf{B}^T\mathbf{B})^{-1} &= \left(\mathbf{V}\boldsymbol{\Lambda}^T\mathbf{U}^T \cdot \mathbf{U}\boldsymbol{\Lambda}\mathbf{V}^T\right)^{-1} = \left(\mathbf{V}\boldsymbol{\Lambda}^2\mathbf{V}^T\right)^{-1} \\ &= \mathbf{V}\boldsymbol{\Lambda}^{-2}\mathbf{V}^T. \end{aligned} \tag{48}$$

Thus,

$$\begin{aligned}\mathbf{B}(\mathbf{B}^T\mathbf{B})^{-1}\mathbf{B}^T &= \mathbf{U}\boldsymbol{\Lambda}\mathbf{V}^T \cdot \mathbf{V}\boldsymbol{\Lambda}^{-2}\mathbf{V}^T \cdot \mathbf{V}\boldsymbol{\Lambda}^T\mathbf{U}^T \\ &= \mathbf{U}\boldsymbol{\Lambda}\boldsymbol{\Lambda}^{-2}\boldsymbol{\Lambda}^T\mathbf{U}^T. \end{aligned} \tag{49}$$

Define $\tilde{\boldsymbol{\Lambda}} = \boldsymbol{\Lambda}(1:L, 1:L)$ as the diagonal matrix with diagonal elements being the eigenvalue of $\mathbf{B}$. Since $\boldsymbol{\Lambda} = [\tilde{\boldsymbol{\Lambda}}, \mathbf{0}]^T$, we have $\boldsymbol{\Lambda}^{-2} = \tilde{\boldsymbol{\Lambda}}^{-2}$ and $\boldsymbol{\Lambda}^T = [\tilde{\boldsymbol{\Lambda}}, \mathbf{0}]$. Also, we can obtain

$$\boldsymbol{\Lambda}\boldsymbol{\Lambda}^{-2}\boldsymbol{\Lambda}^T = \begin{bmatrix} \tilde{\boldsymbol{\Lambda}} \\ \mathbf{0} \end{bmatrix}\tilde{\boldsymbol{\Lambda}}^{-2}[\tilde{\boldsymbol{\Lambda}}, \mathbf{0}] = \begin{bmatrix} \mathbf{I}_{L\times L} & \mathbf{0} \\ \mathbf{0} & \mathbf{0} \end{bmatrix}. \tag{50}$$

Plugging Eq. (50) into Eq. (49) results in:

$$\begin{aligned}\boldsymbol{\Delta}_\mathbf{B} &= \mathbf{I} - \mathbf{B}(\mathbf{B}^T\mathbf{B})^{-1}\mathbf{B}^T \\ &= \mathbf{I} - \mathbf{U}\begin{bmatrix} \mathbf{I}_{L\times L} & \mathbf{0} \\ \mathbf{0} & \mathbf{0} \end{bmatrix}\mathbf{U}^T = \mathbf{I} - \tilde{\mathbf{U}}\tilde{\mathbf{U}}^T. \end{aligned} \tag{51}$$

This proves Eq. (39) from Eq. (36).

References

[1] Cisco, "Cisco visual networking index: Global mobile data traffic forecast update 2014–2019," Cisco, San Jose, CA, USA, White Paper, Feb. 2015.

[2] H. Burchardt, N. Serafimovski, D. Tsonev, S. Videv, and H. Haas, "VLC: Beyond point-to-point communication," *IEEE Commun. Mag.*, vol. 52, no. 7, pp. 98–105, Jul. 2014.

[3] H. Elgala, R. Mesleh, and H. Haas, "Indoor optical wireless communication: Potential and state-of-the-art," *IEEE Commun. Mag.*, vol. 49, no. 9, pp. 56–62, Sep. 2011.

[4] "Visible light communication (VLC)—A potential solution to the global wireless spectrum shortage," GBI Res., London, U.K., Tech. Rep. GBISC017MR, Mar. 2011.

[5] S. Dimitrov and H. Haas, *Principles of LED Light Communications: Towards Networked Li-Fi*. Cambridge, U.K.: Cambridge Univ. Press, 2015.

[6] K.-D. Langer *et al.*, "Optical wireless communications for broadband access in home area networks," in *Proc. 10th Anniversary Int. Conf. Trans. Opt. Netw.*, vol. 4. Jun. 2008, pp. 149–154.

[7] J. Armstrong, "OFDM for optical communications," *J. Lightw. Technol.*, vol. 27, no. 3, pp. 189–204, Feb. 1, 2009.

[8] J. Armstrong and B. Schmidt, "Comparison of asymmetrically clipped optical OFDM and DC-biased optical OFDM in AWGN," *IEEE Commun. Lett.*, vol. 12, no. 5, pp. 343–345, May 2008.

[9] D. J. F. Barros, S. K. Wilson, and J. M. Kahn, "Comparison of orthogonal frequency-division multiplexing and pulse-amplitude modulation in indoor optical wireless links," *IEEE Trans. Commun.*, vol. 60, no. 1, pp. 153–163, Jan. 2012.

[10] T. M. Schmidl and D. C. Cox, "Robust frequency and timing synchronization for OFDM," *IEEE Trans. Commun.*, vol. 45, no. 12, pp. 1613–1621, Dec. 1997.

[11] M. Speth, S. Fechtel, G. Fock, and H. Meyr, "Optimum receiver design for OFDM-based broadband transmission. II. A case study," *IEEE Trans. Wireless Commun.*, vol. 49, no. 4, pp. 571–578, Apr. 2001.

[12] B. Park, H. Cheon, C. Kang, and D. Hong, "A novel timing estimation method for OFDM systems," *IEEE Commun. Lett.*, vol. 7, no. 5, pp. 239–241, May 2003.

[13] S. Tian, K. Panta, H. A. Suraweera, B. Schmidt, S. Mclaughlin, and J. Armstrong, "A novel timing synchronization method for ACO-OFDM-based optical wireless communications," *IEEE Trans. Wireless Commun.*, vol. 7, no. 12, pp. 4958–4967, Dec. 2008.

[14] X. Li, Y. C. Wu, and E. Serpedin, "Timing synchronization in decode-and-forward cooperative communication systems," *IEEE Trans. Signal Process.*, vol. 57, no. 4, pp. 1444–1455, Apr. 2009.

[15] B. Ghimire, I. Stefan, H. Elgala, and H. Haas, "Time and frequency synchronisation in optical wireless OFDM networks," in *Proc. IEEE 22nd Int. Symp. Pers., Indoor Mobile Radio Commun.*, Sep. 2011, pp. 819–823.

[16] A. A. Nasir, H. Mehrpouyan, S. D. Blostein, S. Durrani, and R. A. Kennedy, "Timing and carrier synchronization with channel estimation in multi-relay cooperative networks," *IEEE Trans. Signal Process.*, vol. 60, no. 2, pp. 793–811, Feb. 2012.

[17] Y. Jiang, X. Zhu, E. Lim, Y. Huang, and H. Lin, "Low-complexity semiblind multi-CFO estimation and ICA-based equalization for CoMP OFDM systems," *IEEE Trans. Veh. Technol.*, vol. 63, no. 4, pp. 1928–1934, May 2014.

[18] M. F. G. Medina, O. González, S. Rodríguez, and I. R. Martín, "Timing synchronization for OFDM-based visible light communication system," in *Proc. Wireless Telecommun. Symp. (WTS)*, Apr. 2016, pp. 1–4.

[19] C. Chen, D. A. Basnayaka, and H. Haas, "Downlink performance of optical attocell networks," *J. Lightw. Technol.*, vol. 34, no. 1, pp. 137–156, Jan. 1, 2016.

[20] V. Jungnickel, V. Pohl, S. Nonnig, and C. V. Helmolt, "A physical model of the wireless infrared communication channel," *IEEE J. Sel. Areas Commun.*, vol. 20, no. 3, pp. 631–640, Apr. 2002.

[21] J. M. Kahn and J. R. Barry, "Wireless infrared communications," *Proc. IEEE*, vol. 85, no. 2, pp. 265–298, Feb. 1997.

[22] L. Zeng, D. O'Brien, H. Le-Minh, K. Lee, D. Jung, and Y. Oh, "Improvement of date rate by using equalization in an indoor visible light communication system," in *Proc. IEEE Int. Circuits Syst. Commun.*, May 2008, pp. 678–682.

[23] L. Wu, Z. Zhang, J. Dang, and H. Liu, "Adaptive modulation schemes for visible light communications," *J. Lightw. Technol.*, vol. 33, no. 1, pp. 117–125, Jan. 1, 2015.

[24] D. C. O'Brien, "Visible light communications: Challenges and potential," in *Proc. IEEE Photon. Conf.*, Oct. 2011, pp. 365–366.

[25] D. Tsonev, S. Videv, and H. Haas, "Unlocking spectral efficiency in intensity modulation and direct detection systems," *IEEE J. Sel. Areas Commun.*, vol. 33, no. 9, pp. 1758–1770, Sep. 2015.

[26] H. L. van Trees and K. L. Bell, *Bayesian Bounds for Parameter Estimation and Nonlinear Filtering/Tracking*. Hoboken, NJ, USA: Wiley, 2007.

[27] S. P. Boyd and L. Vandenberghe, *Convex Optimization*. Cambridge, U.K.: Cambridge Univ. Press, 2004.

[28] Y.-C. Wu and E. Serpedin, "Training sequences design for symbol timing estimation in MIMO correlated fading channels," in *Proc. IEEE Global Teleommun.*, Nov. 2004, pp. 81–85.

[29] T. Soderstrom and P. Stoica, *System Identification*. London, U.K.: Prentice-Hall, 1989.

Yufei Jiang (S'12–M'14) received the Ph.D. degree from the University of Liverpool, Liverpool, U.K., in 2014. From 2014 to 2015, he was with the Department of Electrical and Electronic Engineering, University of Liverpool, as a Post-Doctoral Researcher. From 2015 to 2017, he was a Research Associate with the Institutes for Digital Communications, The University of Edinburgh, U.K. He is currently an Assistant Professor with the Harbin Institute of Technology, Shenzhen, China. His research interests include LiFi, DCO-OFDM, synchronization, full-duplex, and blind source separation.

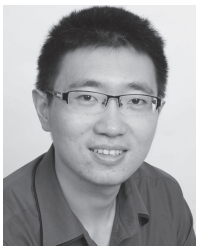

Yunlu Wang (S'14) received the B.Eng. degree in telecommunication engineering from the Beijing University of Post and Telecommunications, China, in 2011, and the double M.Sc. degrees in digital communication and signal processing from The University of Edinburgh, U.K., in 2013, and in electronic and electrical engineering from Beihang University, China, in 2014. He is currently pursuing the Ph.D. degree in electrical engineering with The University of Edinburgh. His research focus is on visible light communication and radio frequency hybrid networking.

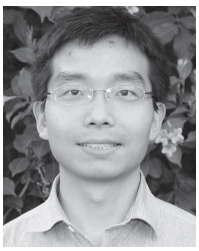

Pan Cao (S'12–M'15) received the B.Eng. degree in mechano-electronic engineering and the M.Eng. degree in information and signal processing from Xidian University, Xi'an, China, in 2008 and 2011, respectively, and the Dr.-Ing (Ph.D.) degree in electrical engineering from TU Dresden, Germany, in 2015. From 2015 to 2017, he was a Post-Doctoral Research Associate with the Institutes for Digital Communications, The University of Edinburgh, U.K., supported by the EPSRC project Seamless and Efficient Wireless Access for Future Radio Networks. He was also a Visiting Post-Doctoral Research Associate with Princeton University during the first three months of 2017. Since 2017, he has been a Senior Lecturer with the School of Engineering and Technology, University of Hertfordshire, U.K. His current research interests include millimeter-wave communication, signal processing for radar and communications, and nonconvex optimization. He received the Best Student Paper Award of the 13th IEEE International Workshop on Signal Processing Advances in Wireless Communications, Cesme, Turkey, in 2012, and the Qualcomm Innovation Fellowship Award in 2013.

Majid Safari (S'08–M'11) received the B.Sc. degree in electrical and computer engineering from the University of Tehran, Iran, in 2003, the M.Sc. degree in electrical engineering from the Sharif University of Technology, Iran, in 2005, and the Ph.D. degree in electrical and computer engineering from the University of Waterloo, Canada, in 2011. Before joining Edinburgh in 2013, he held the prestigious MITACS Elevate Strategic Fellowship at McMaster University, Canada. He is currently an Assistant Professor with the Institute for Digital Communications, The University of Edinburgh. His research interests include optical fiber and optical wireless communications, and signal processing for optical communication systems. He is currently an Associate Editor of the IEEE COMMUNICATION LETTERS. He also served as a Guest Editor of a special issue of the IEEE ACCESS journal on Optical Wireless Technologies for 5G Communications and beyond and was the TPC Co-Chair of the 4th International Workshop on Optical Wireless Communication in 2015.

John Thompson (M'94–SM'13–F'16) currently holds a Personal Chair in signal processing and communications with The University of Edinburgh, U.K. He also leads the European Marie Curie Training Network ADVANTAGE, which trains 13 Ph.D. students in Smart Grids. He has published around 300 papers in these topics and was recognized by Thomson Reuters as a Highly Cited Researcher in 2015 and 2016. His main research interests are in wireless communications, sensor signal processing, and energy-efficient communications networks and smart grids. He was a Distinguished Lecturer on green topics for ComSoc in from 2014 to 2015. He is currently an Editor of the Green Series of the *IEEE Communications Magazine* and an Associate Editor of the IEEE TRANSACTIONS ON GREEN COMMUNICATIONS AND NETWORKS.

Harald Haas received the Ph.D. degree from The University of Edinburgh in 2001, where he currently holds the Chair of mobile communications with The University of Edinburgh. He is also the Initiator, Co-Founder, and Chief Scientific Officer of pureLiFi Ltd. as well as the Director of the LiFi Research and Development Center, The University of Edinburgh. He first introduced and coined spatial modulation and LiFi. He has published 400 conference and journal papers including a paper in Science. He has co-authored a book entitled *Principles of LED Light Communications Towards Networked Li-Fi* published with Cambridge University Press in 2015. His main research interests are in optical wireless communications, hybrid optical wireless and RF communications, spatial modulation, and interference coordination in wireless networks. He was elected as a fellow of the Royal Society of Edinburgh in 2017. He was a co-recipient of recent best paper awards at VTC-Fall in 2013, VTC-Spring in 2015, ICC in 2016, and ICC in 2017. He was a co-recipient of the EURASIP Best Paper Award for the *Journal on Wireless Communications and Networking* in 2015, and a co-recipient of the Jack Neubauer Memorial Award of the IEEE Vehicular Technology Society. In 2012 and 2017, he was a recipient of the prestigious Established Career Fellowship from the Engineering and Physical Sciences Research Council (EPSRC) within Information and Communications Technology in U.K. He is an Editor of the IEEE TRANSACTIONS ON COMMUNICATIONS and the IEEE JOURNAL OF LIGHTWAVE TECHNOLOGIES. In 2014, he was selected by EPSRC as one of ten Recognizing Inspirational Scientists and Engineers Leaders in U.K. In 2016, he received the Outstanding Achievement Award from the International Solid State Lighting Alliance. LiFi was listed among the 50 best inventions in TIME Magazine 2011. He was an Invited Speaker at TED Global 2011, and his talk: Wireless Data from Every Light Bulb has been watched online more than 2.4 million times. He gave a second TED Global lecture in 2015 on the use of solar cells as LiFi data detectors and energy harvesters. This has been viewed online more than 1.8 million times.

AUTHOR QUERIES

AUTHOR PLEASE ANSWER ALL QUERIES

PLEASE NOTE: We cannot accept new source files as corrections for your paper. If possible, please annotate the PDF proof we have sent you with your corrections and upload it via the Author Gateway. Alternatively, you may send us your corrections in list format. You may also upload revised graphics via the Author Gateway.

AQ:1 = Please be advised that per instructions from the Communications Society this proof was formatted in Times Roman font and therefore some of the fonts will appear different from the fonts in your originally submitted manuscript. For instance, the math calligraphy font may appear different due to usage of the usepackage[mathcal]euscript. The Communications Society has decided not to use Computer Modern fonts in their publications.

AQ:2 = Please provide the location and postal code for "University of Hertfordshire."

AQ:3 = Note that if you require corrections/changes to tables or figures, you must supply the revised files, as these items are not edited for you.

AQ:4 = Please provide the white paper no. for ref. [1].

AQ:5 = Please provide the author names for ref. [4].